Advanced steady-state modelling and optimisation of Natural Gas Reforming reactors

Vasco Hugo Coimbra Manaças

Dissertation to obtain the Master of Science Degree in

Chemical Engineering

Examination Committee

Chairperson:	Prof. Dr. Maria Filipa Gomes Ribeiro
Supervisors:	Prof. Dr. Henrique Aníbal Santos de Matos
	Dr. Štěpán Špatenka
Members of the committee:	Dr. Diogo Alexandre Cipriano Narciso
	Dr. Pedro Miguel Gil Castro

December 2013

Para ser grande, sê inteiro: nada
Teu exagera ou exclui.
Sê todo em cada coisa. Põe quanto és
No mínimo que fazes.
Assim em cada lago a lua toda
Brilha, porque alta vive.

Ricardo Reis

Acknowledgements

First of all I would like to acknowledge the contribution of my advisors to this work. I also have to express a few words of gratitude to them: to Prof. Dr. Henrique Matos for his advice and availability to review this dissertation; and to Dr. Štěpán Špatenka for sharing his experience and knowledge, and for always finding the time to answer my questions.

I am grateful for the opportunity I was granted from Instituto Superior Técnico and Process Systems Enterprise Ltd. for working and developing this dissertation in a business environment.

I am also grateful to my friends Francisco, Pedro and Tiago who came with me to London and helped me during our first seven months abroad and to all PSE staff who contributed with a good working environment.

Finally, a kind word of gratitude goes to my close friends and family for all their love and support and for always believing in me.

Vasco H. C. Manaças

Resumo

O reforming de gás natural (NGR) é um sector importante da indústria química. Fornece hidrogénio para a indústria de refinação e é a principal fonte de gás-de-síntese na produção de amoníaco e metanol. A produção de combustíveis *Fischer-Tropsch* tem potencial para se tornar uma aplicação importante. O mercado vai expandir num futuro próximo, logo é importante desenvolver modelos precisos e preditivos para apoio à decisão em síntese e otimização de processos.
Esta dissertação apresenta o desenvolvimento de soluções de modelação do NGR em gPROMS®. Foram modelados dois reatores principais usados no NGR, o reator tubular de *steam reforming* (SMR) e o reator autotérmico (ATR). A biblioteca avançada do gPROMS® para reatores catalíticos de leito-fixo (AML:FBCR) foi usada para modelar os leitos catalíticos em detalhe, considerando rigorosamente o transporte de massa e calor no interior da partícula. Modelos simplificados foram desenvolvidos para modelar a fornalha do SMR e a camara de combustão do ATR.
Dois estudos de caso industriais da literatura foram considerados para validar os modelos. O caso do SMR foi simulado com um perfil de temperatura fixo e com um fluxo de calor calculado pelo modelo da fornalha. Ambas as abordagens produziram resultados concordantes com os dados industriais. O caso do ATR foi simulado com a camara de combustão simplificada, e os resultados apresentam pequenos desvios aos dados industriais, à saída do reator.
As condições do estudo de caso do SMR foram otimizadas maximizando a produção de hidrogénio, obtendo uma eficiência energética inferior (um gasto de mais 0.9 kJ/mol_{H2}).

Palavras chave: Reforming de gás natural, steam reforming, reforming autotérmico, gPROMS, modelação, otimização.

Abstract

Natural gas reforming (NGR) is an important sector.in the chemical and petrochemical industry. It is a source of hydrogen for the refining industry and the main source of synthesis gas for the manufacture of chemicals such as ammonia and methanol. Production of synthetic fuels via Fischer-Tropsch has great potential to become another major application of NGR. Demand for NGR products will be increasing in the near future so it is important to develop accurate and predictive modelling tools for decision support in reactor and process design and operation.

This dissertation presents initial developments on NGR modelling in gPROMS®. The two main reformers, the steam methane reformer (SMR) and the autothermal reformer (ATR) were modelled. The gPROMS® Advanced Model Library for Fixed-Bed Reactors (AML:FBCR) was used for detailed modelling of the catalyst beds considering rigorous intra-particle mass and heat transport. Simplified models were developed for the furnace of the SMR and for the combustion chamber of the ATR.

Two industrial cases from the literature were studied. The one for SMR was simulated with a fixed wall temperature profile and afterwards with heat fluxes calculated from a radiation fired heater model. Both approaches revealed good agreement with plant data. The one for ATR was simulated with the simplified combustion chamber and predictions had only minor discrepancies from plant outlet data.

A set of operational conditions, of the SMR case study, were optimised for maximum hydrogen throughput, at the expense of lower energy efficiency (more 0.9 kJ/mol_{H2} spent).

Keywords: Natural gas reforming, steam methane reforming, autothermal reforming, gPROMS, modelling, optimisation.

Table of Contents

List of Tables

List of Figures

Glossary

AML:FBCR	gPROMS® Advanced Model Library for Fixed-Bed Catalytic Reactors
ATR	Autothermal reforming reactor
BC	Boundary condition
BFW	Boiler feed water
FT	Fischer-Tropsch
gPROMS	general Process Modelling System (gPROMS® ModelBuilber)
GTL	Gas-to-liquids
HER	Heat exchange reforming reactor
KPI	Key performance indicator
NGR	Natural gas reforming
O_2/C ratio	Oxygen to carbon (methane) molar ratio
PML:SS	gPROMS® Steady State Process Model Library
POX	Partial oxidation reaction
S/C ratio	Steam to carbon (methane) molar ratio
SMR	Steam methane reforming reactor
SR	Steam reforming reaction
WGS	Water gas shift reaction
WGSR	Water gas shift reactor

Nomenclature

Latin symbols

A	area	m^2
App	approach to equilibrium	-
E	energy consumption per mol	kJ/mol
F	molar flow rate	mol/s
H	enthalpy flux	J/m^2 s
K	equilibrium or adsorption constant	(bar)
M	mass flux	kg/m^2 s
N	molar flux	mol/m^2 s
P	pressure	bar
Pr	Prandtl number	-
$RRate$	reaction rate	mol/kg_{cat} s
Re	Reynolds number	-
T	temperature	K
V	volume	m^3
av	area-volume ratio	m^2/m^3
d	diameter	m
h	specific enthalpy; heat transfer coeff.	J/kg; W/m^2 K
i	component i	-
j	reaction j	-
k	kinetic constant	(bar) mol/kg_{cat} s
m	mass fraction	kg/kg
p	partial pressure	bar
q	heat flux	J/m^2 s
r	radius	m
u	velocity	m/s
x	molar fraction	mol/mol
z	axial position	m

Greek symbols

ΔG_f	Gibbs free energy of formation	J/mol
ΔH_f	enthalpy of formation	J/mol
ΔP	pressure drop	bar
α	bed-to-wall heat transfer coefficient	W/m^2 K
δ	active layer thickness	m
ε	porosity	void m^3/solid m^3

ν	stoichiometric coefficient	-
ξ	emissivity	-
ρ	volumetric mass	kg/m^3
σ	Stefan-Boltzmann constant	J/m^2 s K^4

Subscripts and Superscripts

0	pure component, standard state
ac	active layer
adj	adjustable
adv	advective
b	bed
$conv$	convective
$corr$	corrected
$diff$	diffusive
$disp$	dispersive
e	effective
eff	effective
eq	equilibrium
f	fluid
i	inner; component i
in	inlet
o	outer
out	outlet
p	pellet
r	radial
s	solid
t	tube
tot	total
w	wall
z	axial

1 Introduction

Natural gas reforming (NGR) is a key sector in the chemical and petrochemical industry. It is the main route to hydrogen and synthesis gas manufacture. Hydrogen and synthesis gas are a path to a wide range of applications: hydrogen is extensively used in the refinery for hydrotreatment and hydrocraking operations helping produce cleaner fuels; synthesis gas can be used in ammonia production, methanol production and fuel production in gas-to-liquids (GTL) plants.

Environmental awareness is leading fuel regulations towards stricter limits on impurities and aromatics. This is starting to cause a severe increase on refinery hydrogen demands: hydrotreatment units will require more hydrogen while in catalytic reforming aromatics formation will be reduced and consequently hydrogen co-production will also be reduced [1]. GTL is also an interesting source of clean, high quality fuels that can be blended with refinery fuels to meet all the regulatory requirements [1,2].

On the supply side, natural gas is definitely the major feedstock for hydrogen and synthesis gas production although it also plays a key role on the world primary energy supply, with a share of 21.4% in 2010 [3]. Environmental awareness also turned associated gas flaring in oil extraction fields an outdated practice. Shale and tight gas are becoming a relevant supply source, namely in the United States of America [4]. These alternative gas sources are usually in remote locations and are also called stranded gas sources. Conversion from gas to liquids will allow its transport from stranded locations to the relevant markets in the existing liquid fuel transport infrastructure, removing the need to create new gas transport pipelines [5].

NGR processes have long been established since Haldor Topsoe built their first steam methane reformer in 1957 and the first autothermal reformer in 1958 [6]. Since then other type of reformer reactors appeared like the gas heated or heat exchanging reformer. And nowadays there are still important developments under way: new reactor designs are being developed with higher heat fluxes or energy efficiency; process configurations combining different reformers together are being studied and were already successfully implemented.

During these 50 years of process some work was made on mathematical modelling of reformer reactors. Reaction kinetics were studied by various authors, Hughes and Avetisov [7,8] reviewed previous studies and also developed their own models, but the most widely used kinetic model is the one developed in 1989 by Xu and Froment [9]. The tubular steam reformer and its firebox [10–16], the autothermal reformer [17–21] and even the heat exchanging reformer [22–24] were all subject of modelling research. Optimisation studies are also reported in the past 10-15 years [25–31].

All these modelling efforts approached the fixed-bed reactor using one-dimensional bed models. Diffusion inside the catalyst particles was sometimes modelled explicitly, accounting for component diffusion through catalyst pores; and other times implicitly, using an effectiveness factors and the Thiele modulus. These are important assumptions that, to the best of my knowledge, were not validated on any publication until now. In my understanding, these assumptions are made because of

(i) the computational effort required to solve the more detailed models; (ii) the complex nature of the phenomena involved (diffusivity calculations and mass transfer inside the catalyst pellet, radial heat transfer inside the reactor and on the furnace side); (iii) there is few industrial data publicly available.
Detailed and accurate modelling of natural gas reformers would give better insight into process design and operation [32,33]. This type of predictive modelling would allow optimisation of both reactor and processes and would be a very useful tool for making decisions in this sector.

1.1 Motivation / Purpose

Growth in hydrogen and synthesis gas production sector is being pulled by demand and pushed by supply. Natural gas reforming developments strive to deliver more economic and larger plants than ever before. Advanced process modelling can bring more leverage to seize growth opportunities by helping managers and engineers to make informed process innovation, design and operation decisions.
The objective of this work is to start developing modelling solutions for natural gas reforming with the purpose of, in the future, creating a comprehensive accurate and predictive modelling pack for synthesis gas manufacture in gPROMS®.

1.2 Outline

Chapter 2 includes a literature review on natural gas reforming. NGR applications and feedstocks are reviewed.
Chapter 3 describes the models used and developed during this work.
Chapter 4 presents the simulation results of two industrial cases using the developed models for the steam methane reformer and the autothermal reformer.
Chapter 5 presents the optimisation results of the steam methane reformer case study.
Finally, chapter 6 summarises the conclusions of this work, referring what was achieved and possible future work is discussed.

2 Natural Gas Reforming

This chapter reviews natural gas reforming (NGR) processes, chemistry design and operation. Possible product gas applications and available feedstocks are discussed. Chemical routes to hydrogen and carbon monoxide synthesis gas are explained, along with possible undesirable reactions. Equipment used in NGR is presented, first different possible reactor designs, and then equipment related to feed gas pre-treating, product gas composition adjustment and cleaning. Finally some process flow diagrams are included. A more in-depth review of this subject can be found in [32,34,35].

2.1 Applications

NGR produces hydrogen, mainly for refinery hydrotreating and hydrocracking, and various types of synthesis gas. Synthesis gas, also called syngas, is considered to be a mixture of hydrogen, carbon-oxides and, in some cases, nitrogen. Syngas major applications are ammonia and methanol manufacture, while the production of synthetic flues, via Fischer-Tropsch (FT) synthesis, is another growing application. Other minor applications worth mentioning are higher alcohols and iron ore reduction gas production [36].

Syngas composition changes for each respective application and can be characterised by a specific stoichiometric ratio. Ammonia synthesis gas requires a H_2/N_2 ratio of 3.0; methanol a ratio, or module, $M=(H_2-CO)/(CO+CO_2)$ of 2.0; low temperature FT a H_2/CO ratio of 2.0 and high temperature FT an M module of 2.0 [32,34].

2.2 Feedstocks

Natural gas is the main feedstock for hydrogen and syngas production [32,35]. Possible hydrocarbon feedstocks can range up to naphtha with boiling points around 200 °C. Hydrogen-rich off-gas (e.g. from the refinery) can be added as a co-feedstock and lower alcohols like methanol can, in some cases, be used also.

The usual reforming agent is steam, oxygen or air but alternative compounds like carbon dioxide or even methanol can be used [36]. The choice of reforming agent will depend on the reactor used and on the desired outlet syngas composition: steam increases the H_2/CO ratio while carbon dioxide decreases it.

Heavier naphtha and higher hydrocarbons like crude oil and coal are also suitable feedstocks for syngas production but require other, usually more expensive, gasification processes that are not discussed here.

2.3 Chemical Routes

In a natural gas reforming process stable molecules (mainly methane), need to be broken into less stable, highly reactive molecules like hydrogen and carbon monoxide. To accomplish this there are two main routes: steam reforming and partial oxidation.

Methane steam reforming produces a hydrogen and carbon monoxide with ratio of 3.0. Higher hydrocarbons react in a similar way to the steam reforming reaction (SR).

$$CH_4 + H_2O \rightleftarrows CO + 3\,H_2, \qquad \Delta H^0 = 206\ kJ/mol \tag{2.1}$$

$$C_nH_m + n\,H_2O \rightarrow n\,CO + (n+\frac{m}{2})\,H_2, \qquad \Delta H^0 > 0 \tag{2.2}$$

Along with the SR, water gas shift reaction (WGS) also occurs.

$$CO + H_2O \rightleftarrows CO_2 + H_2, \qquad \Delta H^0 = -41\ kJ/mol \tag{2.3}$$

When carbon dioxide is used as a reforming agent, the reaction is the difference between (2.1) and (2.3).

$$CH_4 + CO_2 \rightleftarrows 2CO + 2\,H_2, \qquad \Delta H^0 = 247\ kJ/mol \tag{2.4}$$

These reactions are all reversible with exception for steam reforming of higher hydrocarbons and all of them require a catalyst, typically supported nickel.

Some natural gas reforming processes take advantage of partial oxidation of hydrocarbons (POX) which is an irreversible process. The reactions may, or may not require a catalyst, typically nickel supported.

$$\begin{gathered} CH_4 + \tfrac{1}{2}\,O_2 \rightarrow CO + 2\,H_2 \\ \vdots \\ CH_4 + 2\,O_2 \rightarrow CO_2 + 2\,H_2O \end{gathered} \tag{2.5}$$

2.3.1 Undesired reactions

The main problem faced by natural gas reformers is carbon formation in the form of coke or soot. And it can be formed from one of the following reactions:

$$2\,CO \rightleftarrows C + CO_2, \qquad \Delta H^0 = -172\ kJ/mol \tag{2.6}$$

$$CH_4 \rightleftarrows C + 2\,H_2, \qquad \Delta H^0 = 75\ kJ/mol \tag{2.7}$$

$$C_nH_m \rightarrow n\,C + \frac{m}{2}\,H_2 \tag{2.8}$$

In steam reformers carbon deposition, (2.7) and (2.8), is the main source of fixed carbon. It usually occurs more at the beginning of the reactor where hydrocarbon concentrations are high and the reaction system is far from equilibrium [36]. High steam to carbon (S/C) ratios were used to avoid coking reactions but recently developed high activity catalysts minimized this issue.

Reaction (2.6) is known as the Boudouard reaction. This reaction is responsible for metal dusting corrosion caused by carbon monoxide rich gases because it can be catalysed by metal surfaces. When metal surface is unprotected severe corrosion can occur [35].

Carbon formation can also occur via thermal cracking of higher hydrocarbons at temperatures above 550 °C. The introduction of pre-reforming[1] minimizes this issue by removing higher hydrocarbons from the main reformer [36].

Other sources of undesirable reactions are sulphur poisoning and sintering of the catalyst [32,34].

[1] Vide page 8.

2.4 Reactors

The main, and most wide-spread, reactor designs for NGR are steam methane reforming (SMR) and autothermal reforming (ATR). Other important reforming technologies include catalytic and non-catalytic partial oxidation and, more recently developed, heat exchange reformers (HER) and oxygen membrane reformers.

Two-step or combined reforming reactors are also important reactor configurations. Two of the referred reactors, usually ATR, SMR or HER, are arranged in series or parallel.

2.4.1 Steam methane reformer – SMR

As the name suggests, the steam methane reformer (SMR) follows the SR reactions. This reformer is often called tubular fired reformer because of the reactor design: catalyst filled tubes placed inside a fired heater, or furnace.

In SMR the reaction proceeds inside a number of reformer tubes while heat is being transferred from the radiant chamber of the furnace. This radiant chamber has burners installed on the walls where the fuel is burned releasing heat. Only 50% of this heat is transferred to the reformer tubes, the remainder is recovered on the convection section of the furnace for pre-heating duties and steam generation. Flue gas temperatures are brought down close to 200 °C and overall thermal efficiencies of 95% can be attained [35,36].

Different burner arrangements are possible (Figure 2.1) and lead to different furnace configurations: top fired; bottom fired; terrace wall fired; or side fired. The side fired reformer furnace is the one which offers more flexibility in design and operation allowing tight control of wall temperatures and achievement of high average heat fluxes [35].

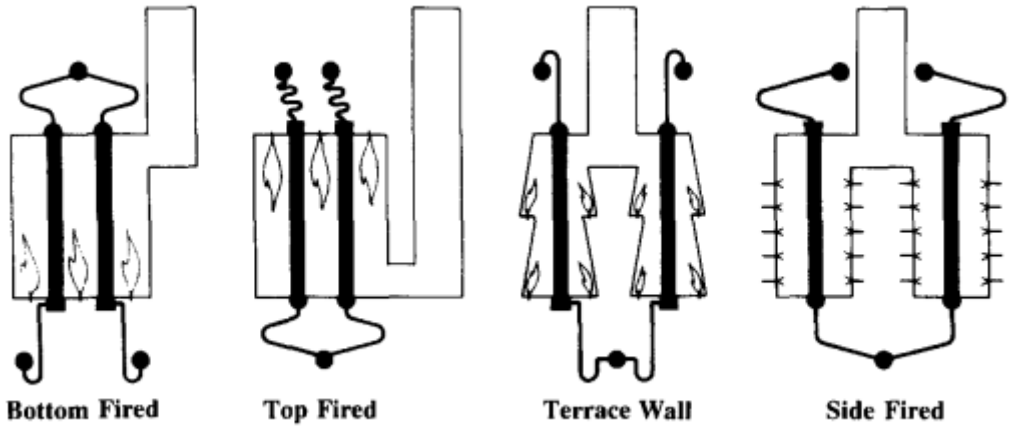

Figure 2.1 Typical configurations of reformer furnace [35]**.**

Typical SMR catalysts are nickel (~9%) supported on alumina carrier. These catalysts are designed for optimal heat transfer and minimal pressure drop and usually are hollow cylindrical pellets with 10-20 mm of outer diameter and one or more holes [34,36]. These catalysts are capable of performing continuous operation in excess of five years [37].

Reformer tubes can have inner diameters of 75-125 mm, with a thickness of 12-25 mm and fired lengths of 9-15 m [1,36]. Operation conditions are limited by tube material maximum allowed

temperature and increasing this temperature will decline expected tube lifetime. Recent metallurgical developments allow maximum tube wall temperatures of 1050 °C [35].

Since most reformers operate near or at equilibrium outlet conditions, the key variables that define outlet gas composition are: hydrocarbon feed composition, inlet S/C ratio, outlet temperature and pressure. Typical conditions are inlet S/C ratios of 2-5, operating pressures of 10-40 bar and outlet temperatures of 800-950 °C. Inlet temperatures to the reformer tubes are limited by thermal cracking of higher hydrocarbons so the typical range is 450-550 °C [1,33,36]. The upper limit rises up to 650 °C when a pre-reformer is installed[2].

Lower S/C ratios are desirable for some applications that require lower H_2/CO ratios. Lower steam contents increase carbon monoxide content at the outlet of water gas shift reactors but also decrease methane conversion. Outlet reformer temperatures can be increased to compensate this decline[35].

Low S/C ratios also lead to lower capital investment and better energy efficient plants. Reactor and heat exchanging equipment size is reduced; and flowrates are also reduced leading to lower compression and heat duties [34].

Synthesis gases produced by SMR from natural gas have H_2/CO ratios between 2.8 and 4.8 [34].

2.4.2 Autothermal reformer – ATR

An autothermal reformer (ATR) is a refractory lined vessel composed by a burner, a combustion chamber and a catalyst fixed-bed. As the name suggests, the reformer is thermally self-sufficient and operates adiabatically with exothermic POX reactions providing the necessary heat for the endothermic SR reactions.

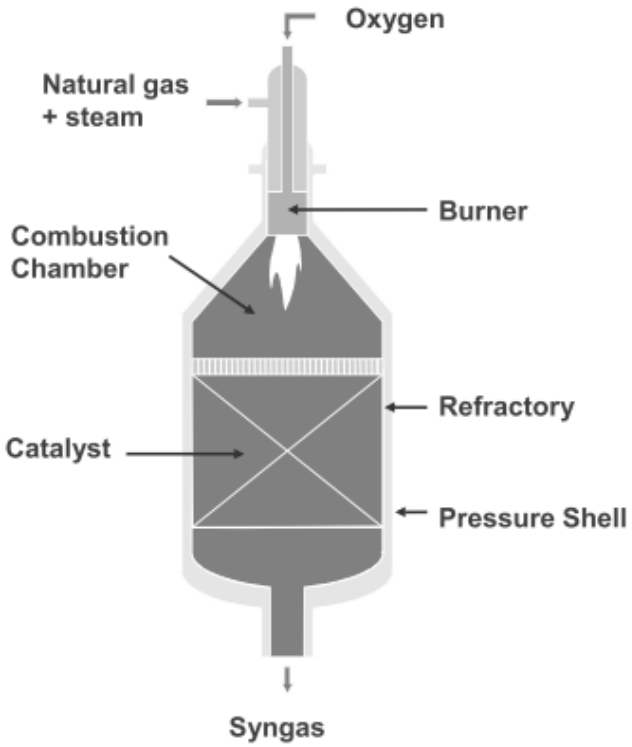

Figure 2.2 ATR illustration [32]**.**

[2] Vide page 8.

Figure 2.2 illustrates an autothermal reformer. Two streams are fed to the reformer, one is the feed gas to be reformed, with a possible addition of steam, and the other must be an oxidant for the POX reactions. These two streams are mixed and fed to the combustion chamber through the installed burner and ignite. Partial combustion reactions occur (POX reactions) and flame temperatures over 3000 °C can be achieved [36]. These high temperatures promote SR reactions in homogeneous phase decreasing gas temperatures due to their endothermic heat of reaction; gas temperatures at catalyst bed inlet reach 1100-1300 °C [32]. The gas mixture at the inlet of the catalyst section is composed of hydrogen, carbon monoxides, steam and unconverted hydrocarbons. At this lower temperature homogeneous SR reactions no longer occur and the catalyst becomes essential to the heterogeneous SR reactions. The catalyst section brings the mixture to equilibrium, and also stabilises the syngas by removing any soot precursors formed in the combustion chamber; gas outlet temperatures are tipically of 900-1100 °C [32].

The feed gas can be imported natural gas, or partially reformed gas (e.g. in a primary reformer) containing a mixture of synthesis gas, steam and unreacted hydrocarbons. These two possibilities are usually distinguished into two different categories: standalone autothermal reformer; and secondary reformer. Although the concept is the same feed conditions and flowrate are be quite different, requiring different burner and reactor design [35].

The oxidant used can be pure oxygen or (enriched) air and both have advantages and draw backs. Air fuelled ATR eliminates the air separation unit that accounts for 30-40% of plant capital costs [6], but will impose once-through operation, larger equipment and higher compression duties. Oxygen fuelled ATR will require an air separation unit but operational costs usually compensate. In fact, for hydrogen productions above 200,000 Nm^3/h oxygen-blown ATR becomes the more economical than SMR because of different economies of scale between the SMR reactor and the air separation unit. Air-blow ATR is used only when nitrogen is needed in the syngas such as in ammonia production

ATR reforming of natural gas can provide lower H_2/CO outlet ratios (1.8-3.8) than SMR due to the introduction of oxygen instead of steam [34].

Typical operating pressures are higher than for SMR and can reach 30-40 bar [36], or even 40-50 bar for oxygen-blown ATR where higher temperatures can be reached and compensate the undesired pressure effect on methane conversion [33]. Oxygen is fed at sub-stoichiometric conditions, typically at oxygen to methane ratios (O_2/C ratios) of 0.5-0.6 [6,33]. Carbon free operation requires a small amount of steam corresponding to S/C ratio lower than 1.0.

Catalyst pellets typically used in ATR are hollow ring-shaped pellets (Raschig rings) of 16 mm in diameter and height with a 6-8 mm hole. Nickel is used at 3-12% in alumina support [36]. These catalysts are designed for high thermal stability, sufficient activity to reach equilibrium and low pressure drop to avoid process gas bypassing through the refractory layer [32]. Operational ATR temperature conditions are limited by the catalyst thermal stability and usually a protective layer of tiles and/or inert catalyst is placed above the catalyst pellets.

2.4.3 Other reformers

Other reformer options are catalytic and non-catalytic partial oxidation, heat exchanging type reformers and oxygen membrane reformers.

The first two are quite different from the concepts here presented and are more used for heavier hydrocarbon feedstocks and will not be described here. More information on non-catalytic partial oxidation can be found in [36] and on catalytic-partial oxidation in [32].

Oxygen membrane reformers are a very recent development and are not commercially available yet. They try to couple the air separation unit and the catalytic reactor for steam reforming by attaching a membrane to the catalyst bed where air flows on one side and the hydrocarbon feed on the other side. Oxygen permeates through the membrane reacting on the catalyst side [32].

The concept of heat exchanging reformers (HER) uses hot gases to provide the heat necessary for reaction. They resemble the SMR in the way the reformer tube side is basically the same, only the furnace gets replaced by a convective chamber. Up until now three different design concepts have been developed and commercialised. Figure 2.3 illustrates these three concepts, A and B can be used as standalone reformers and with any type of heating gas while C needs another reformer working in parallel. This type of reformer can be used alone where usually a fired heater is used to provide the hot flue gases like in Haldor Topsoe's convective reformer [38] or in association with and ATR or SMR.

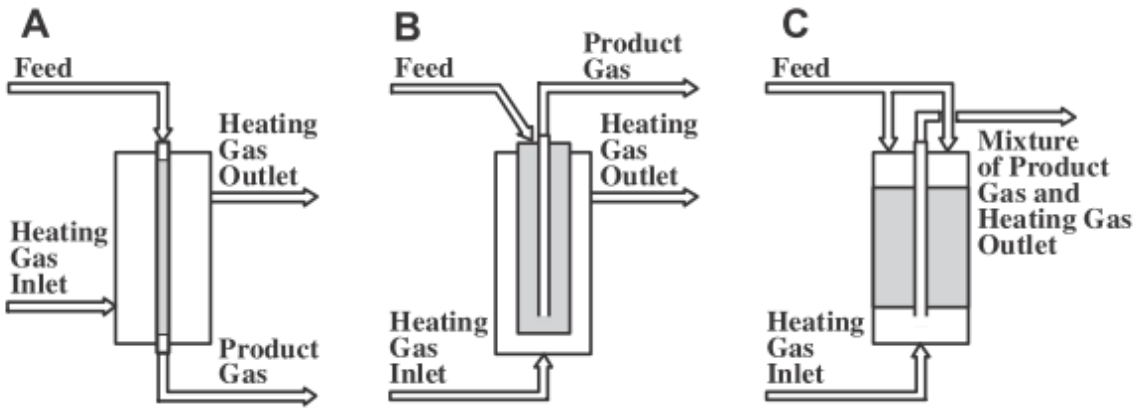

Figure 2.3 Heat exchanging reformer concepts from [32]. A, once-through tubes; B, Bayonet tubes; C, mixing feed and heating gas.

Heat exchanging reformers can operate at process gas and flue gas outlet temperatures of 600 °C and use up to 80% of the fired duty for reaction. This is a big advantage over the SMR reformer and can be an option with lower steam production. The main problem faced in HER is metal dusting corrosion previously explained in section 2.3.1.

Finally the concept of combined reforming also deserves some attention. The most used reformers for NGR can be placed together, in series or parallel, to achieve more flexible operation and better economies of scale. A typical arrangement involves using SMR as a primary reformer and ATR as secondary reformer. In ammonia production this is used with air-blown ATR and in methanol production with oxygen-blow ATR; examples can be found in [35]. HER can also be used in this type of configuration that is thoroughly described in [32].

2.5 Related Equipment

2.5.1 Pre-treatment

Sulphur acts as poison to nickel containing catalysts and is the main contaminant present in hydrocarbon feeds which needs to be removed. This is accomplished by a hydrodesulphurisation unit, followed by H_2S removal over ZnO absorption beds. A more detailed description of these two processes can be found in [32].

2.5.2 Pre-reforming

Pre-reformers are adiabatic steam reforming reactors filled with high activity catalysts used to convert higher hydrocarbons to hydrogen, carbon monoxide and methane. The catalyst used also absorbs the trace amounts of sulphur from the pre-treatment section, thus protecting the main reformer.

Installation of a pre-reformer reduces the risk of carbon formation on the SMR by removal of all higher hydrocarbons and acting as a shield from sulphur poisoning that could reduce catalyst activity at the inlet of this primary reformer. By removing higher hydrocarbons it allows to increase the inlet temperature to the primary reformer up to 650 °C. This also reduces the heat load on the primary reformer, increasing plant energy efficiency. Installation before an ATR will also allow higher inlet temperature and will reduce oxygen consumption significantly [32].

The catalysts used are highly active (30-70% wt.) nickel over alumina support with high specific surface [36]. Small cylindrical pellets with 3-5 mm diameters are used to minimise diffusion restrictions. Pressure drop is low in spite of such small sized particles because of operation at lower temperatures than SMR [32].

Typical inlet temperatures are 350-550 °C [32] and outlet bed temperature will depend on the feed composition, for natural gas a temperature drop of 25-40 °C is expected [36].

2.5.3 WGSR

Water gas shift reactors (WGSR), also known as shift converters, are used to control final gas composition by maximising hydrogen production and removing carbon monoxide.

The WGS reaction is exothermic and these reactors are usually operated adiabatically so inter-stage cooling is required. In these stages heat is recovered by steam production.

Further information regarding the difference between high temperature and low temperature shift converters, the different catalysts used can be found in [32]. A thorough review of reaction mechanism and kinetics is given in [39].

2.5.4 Final gas cleaning

Complete removal of carbon oxides is sometimes required (e.g. ammonia synthesis). For pure hydrogen other contaminants also need to be removed.

Even after the WGSR section trace amounts of carbon monoxide may be present. Methanation, the reverse SR reaction, is sometimes used for this end.

Carbon dioxide removal can be accomplished by CO_2 absorption or by pressure swing adsorption (PSA). Even after the CO_2 absorber section, trace amounts of carbon monoxide may be present and methanation, the reverse SR reaction, is usually used to further reduce the content of carbon oxides.

PSA technology is, at the moment, the preferred process unit for hydrogen clean-up from carbon oxides and unreacted methane because it eliminates the methanation unit and the low temperature WGSR [37]. The off-gas from the PSA unit is used as fuel in the reformer furnace to reduce global fuel consumption.

2.6 Process flow diagrams

Finally two examples of a typical NGR plant for production of hydrogen and ammonia synthesis gas are illustrated.

Figure 2.4 illustrates a hydrogen production plant with SMR. The feed gas is pre-treated in a desulfurizer and after the reformer a high temperature shift converter is used with a final PSA unit for purification.

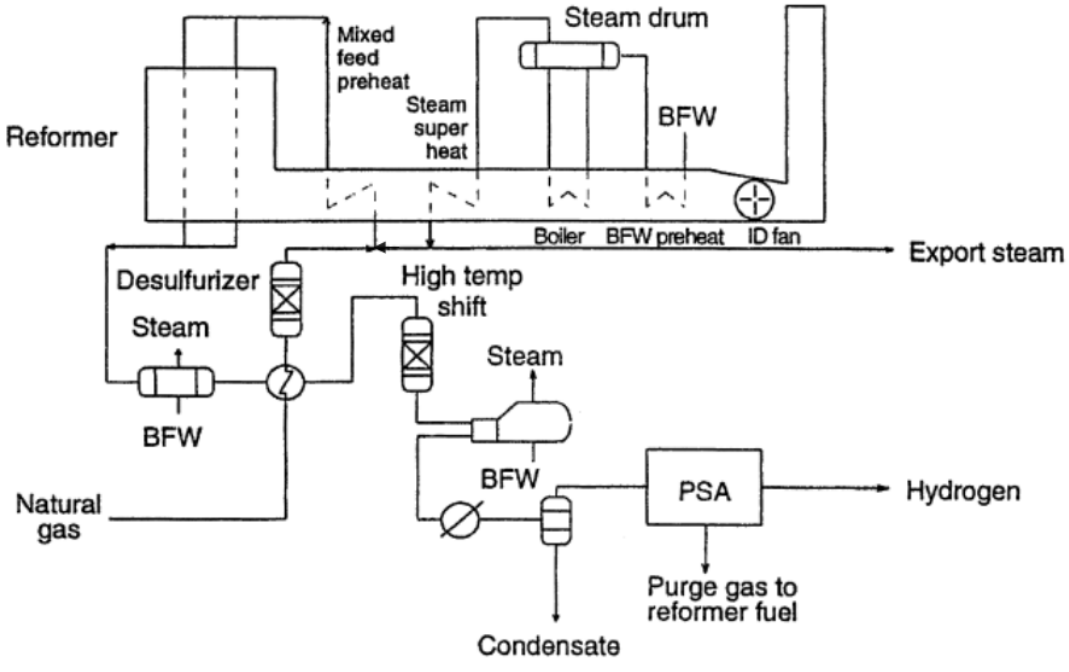

Figure 2.4 Illustration of hydrogen production process flow diagram with SMR [35]**.**

Figure 2.5 illustrates an ammonia synthesis gas plant with combined reforming where the secondary reformer is an ATR. After pre-treatment the natural gas feed is subjected to adiabatic pre-reforming and then is reformed in a SMR before an air-blown ATR. The final gas proceeds to shift converters and heat recovery section.

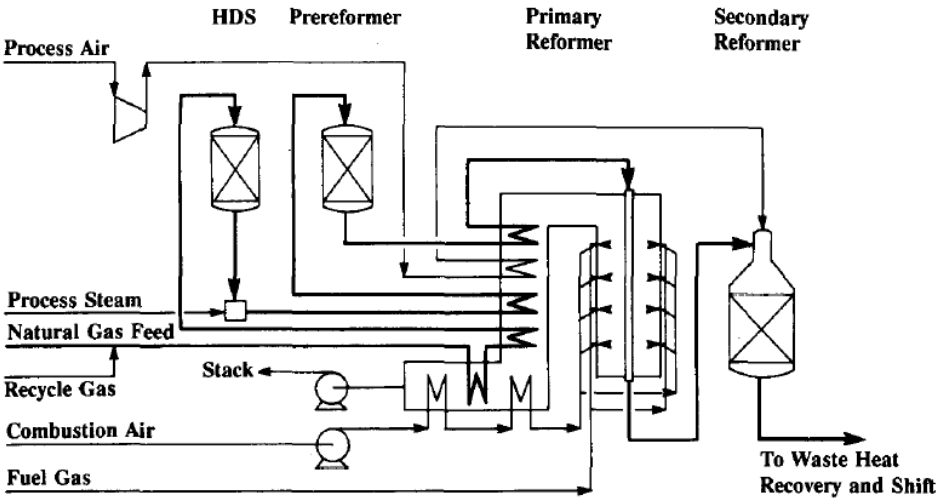

Figure 2.5 Illustration of ammonia synthesis gas production process flow diagram with ATR as a secondary reformer [35]**.**

3 Modelling

This chapter explains the models used in this work as well as some of the modelling decisions that were made. The first section briefly describes the gPROMS® library models and the physical properties package used. The following two sections describe the models developed for the chosen NGR reformers. During literature review, the SMR and ATR reformers proven to be the obvious choice for modelling, not only because these technologies have been established for decades, but also because they are still the main choice for NGR processes. Modelling the HER would be the next logical choice.

3.1 gPROMS® tools

Two gPROMS® libraries were used in the course of this work. The Advanced Model Library for Fixed-Bed Catalytic Reactors (AML:FBCR) was used to model the catalytic part of the reactors and the Process Model Library for Steady State (PML:SS) was used to model the combustion zone of the ATR.

3.1.1 Advanced Model Library for Fixed-Bed Catalytic Reactors – AML:FBCR

The gPROMS® Advanced Model Library for Fixed-Bed Catalytic Reactors (AML:FBCR) was used to model the catalytic sections of the reformer reactors.

This library splits the catalytic reactor model into two main sub-models: the catalytic bed model and the pellet model. Catalytic beds are modelled with one or two dimensional approaches, considering only the axial distribution, or both axial and radial distributions. The pellet can be modelled using a pseudo-homogeneous approach (with an effectiveness factor) or using a one dimensional approach by distributing the model along the pellet diffusion path.

Mass and heat transport phenomena inside catalyst-filled beds can't be accurately predicted from first principles, so an effective approach is considered using semi-empirical parameters, like effective bed conductivity and wall-to-bed heat transfer coefficient. The one dimensional pellet model, on the other hand, considers rigorous mass and heat transfer inside along the pellet diffusion path.

The library also provides models for ancillary equipment like distributor, aggregator and various cooling sections.

The two main reactor models used in this work were the one and two dimensional catalyst beds with one dimensional pellet: *Catalyst_Pellets_Section* (Figure 3.2) and *Catalyst_Pellets_Section_1D_Adiabatic* (Figure 3.1). These two models conjugate the rigorous mass and heat transport phenomena inside the catalyst pores with the respective effective phenomena.

The *Catalyst_Pellets_Section_1D_Adiabatic* model in Figure 3.1 thus considers two different dimensions, or distribution domains:

- Bed axial domain;
- Pellet radial domain.

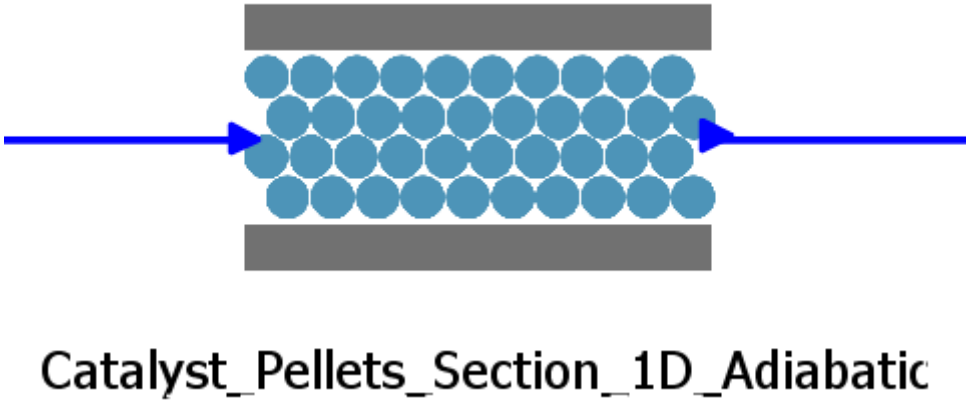

Figure 3.1 AML:FBCR Catalyst_Pellets_Section_1D_Adiabatic model.

The *Catalyst_Pellets_Section* model in Figure 3.2 considers three different dimensions, or distribution domains:

- Bed axial domain;
- Bed radial domain;
- Pellet radial domain.

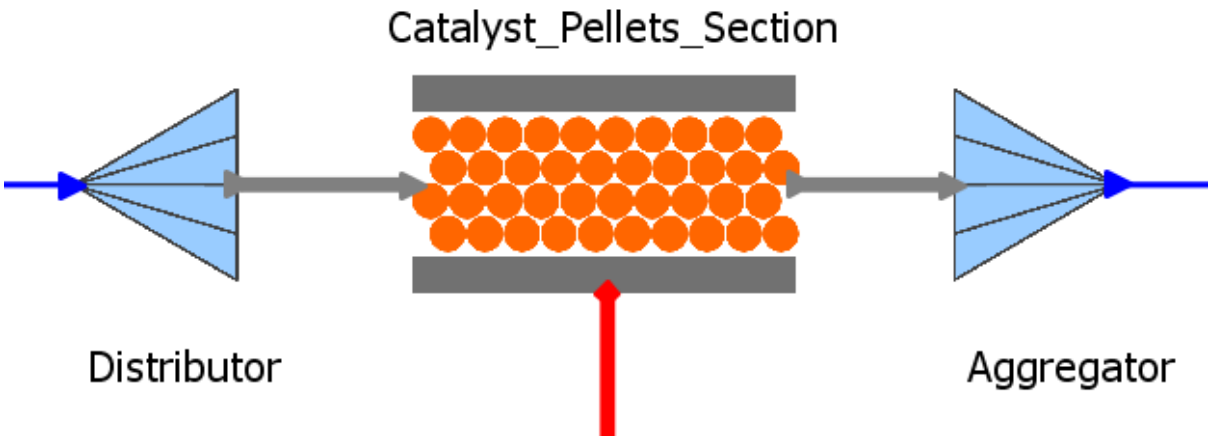

Figure 3.2 AML:FBCR Catalyst_Pellets_Section model with Distributor and Aggregator.

In order to introduce the radial dimension to the model variables a *Distributor* and an *Aggregator* models are required (see Figure 3.2). The *Distributor* transforms the inlet stream variables (blue arrow) into radially distributed variables (grey arrow) assuming uniform distribution while the *Aggregator* does the opposite, acting as a collector unit.

The library uses a set of user-specified auxiliary sub-models for properties and kinetics calculations. These are presented in Table 3.1 with a brief description of each model's main role.

Table 3.1 AML:FBCR reactor auxiliary sub-models and their main functionalities.

Sub-model	Main functionalities
Properties and parameters	• Binary diffusivities calculation
Fluid properties	• Enthalpy calculations • Concentration calculations
Bed properties	• Pressure drop correlations • Mass transfer correlations • Heat transfer correlations
Reaction kinetics	• Reaction stoichiometry • Reaction rates

There are some options available (see Table 3.2) for heat and mass transfer methods and enthalpy calculations that need to be defined for each reactor model. The radial heat transfer option defines how the heat is radially transported (through fluid, solid or both). Intra-particle diffusion can use Fick's law for binary systems or Maxwell-Stefan equations for multi-component diffusion systems; the standard Maxwell-Stefan equations account only for molecular diffusion, while the Dusty-gas (also known as Extended Maxwell-Stefan) also accounts for Knudsen diffusion (which is relevant when the mean free path between molecules becomes much larger than pore size). Finally, mass and heat transfer coefficients, on the gas film outside the particle, are predicted using the provided correlations.

Table 3.2 AML:FBCR reactor model methods.

Method	Options
Radial heat transfer media[1]	• Solid only • Solid and fluid • Fluid only
Partial enthalpy	• Ideal mixture • Real mixture
Intra-particle diffusion	• Maxwell-Stefan model • Dusty-gas model • Fick model
Extra-particle mass and heat transport	• Hougen (1961) correlations • Gnielinski (1982) correlations

The methods used and the customisations made to sub-models are explained below under the reformer model description in section 3.2.1.

3.1.1.1 Two-dimensional fixed-bed with one-dimensional pellet reactor model general equations

A full description of the AML:FBCR models equations will not be presented because these models were not developed during the course of this work and because of intellectual property rights. The

[1] Only used for the two-dimensional bed model.

general, main equations of a steady-state, two dimensional fixed-bed reactor model, with one dimensional pellet model will be briefly described.

A detailed description of the Maxwell-Stefan equations for pellet diffusion falls out of the scope of this work; they are explained in sec. 3.4 of [40]. Other similar heterogeneous reactor models are described in sec. 11.9 and 11.10 of [40].

On the bed model, the momentum balance uses the Ergun correlation to account for pressure drop through packed beds. The equation relates pressure (in Pa), P, with fluid superficial velocity, u_z, bed porosity, ε_b, and particle Sauter equivalent diameter, d_p.

$$-\frac{dP(z)}{dz} = 150\frac{(1-\varepsilon_b)^2\,\mu\,u_z(z,r)}{{\varepsilon_b}^2\,{d_p}^2} + 1.75\frac{(1-\varepsilon_b)\,\rho\,u_z(z,r)^2}{{\varepsilon_b}^3\,d_p} \tag{3.1}$$

The continuity equation for each component, i, accounts for mass convection in both axial and radial directions; mass diffusion in the radial direction and mass transfer from the pellet to bulk fluid from both convection and diffusion. The variables denote mass fluxes, M, in both radial, r, and axial, z, directions; and molar fluxes, N, in pellet radial direction, r_p; these pellet fluxes are at pellet surface, R_p; and the area-to-volume ratio of the bed, av_b, defines the catalyst surface are available.

$$\begin{aligned}\frac{\partial}{\partial z}M_{z,i}^{conv}(i,z,r) + \frac{1}{r}\frac{\partial}{\partial r}[r\,M_r^{conv}(z,r)\,m(i,z,r)] + \frac{\varepsilon_b}{r}\frac{\partial}{\partial r}\left[r\,M_r^{diff}(i,z,r)\right] \\ - M_w(i)\left[N_{r_p}^{conv}(z,r)x_p\left(i,R_p,z,r\right) + \varepsilon_p N_{r_p}^{diff}\left(i,R_p,z,r\right)\right]\,av_b = 0\end{aligned} \tag{3.2}$$

The overall mass continuity equation handles bulk fluid transport conservation in both axial and radial directions.

$$\frac{\partial}{\partial z}M_z^{conv}(z,r) + \frac{1}{r}\frac{\partial}{\partial r}[r\,M_r^{conv}(z,r)] = 0 \tag{3.3}$$

The fluid energy balance equation accounts for axial and radial advection[2] of heat; radial dispersion[3] and diffusion[4] of heat; and also for the heat transfer from catalyst pellets from convection[5] and diffusion. The balance is written using heat fluxes, H.

$$\begin{aligned}\frac{\partial}{\partial z}H_z^{adv}(z,r) + \frac{1}{r}\frac{\partial}{\partial r}[r\,H_r^{adv}(z,r)] + \frac{\varepsilon_b}{r}\frac{\partial}{\partial r}\left[r\,H_r^{disp}(z,r)\right] + \frac{1}{r}\frac{\partial}{\partial r}\left[r\,H_r^{diff}(z,r)\right] \\ - \left[H_{r_p}^{adv}\left(R_p,z,r\right) + H_{r_p}^{disp}\left(R_p,z,r\right) + H_{r_p}^{diff}\left(R_p,z,r\right)\right]\,av_b = 0\end{aligned} \tag{3.4}$$

Inside the catalyst particle the species continuity equation is written in amount of substance units (molarity) and accounts for convective and diffusive transport as well as for any consumption or formation by reaction. The variables denote reaction rates, $RRate$, and stoichiometric coefficients, ν, for each reaction, j, in the system; pellet porosity, ε_p, replaces bed porosity. The Maxwell-Stefan equations are used with this equation to solve the diffusive and convective mass transfer inside the particle.

[2] Advection is the transport of a conserved quantity with mass convection.

[3] Dispersion is used here as the transport of a conserved quantity with mass diffusion.

[4] Diffusion or conduction of heat refers to the molecular diffusion of heat.

[5] Convection is the sum of both advection and dispersion.

$$\frac{1}{r_p}\frac{\partial}{\partial r_p}\left[r_p\, N_{r_p}^{conv}(r_p,z,r)\, x_p(i,r_p,z,r)\right] + \frac{\varepsilon_p}{r_p}\frac{\partial}{\partial r_p}\left[r_p\, N_{r_p}^{diff}(i,r_p,z,r)\right] = \sum_j \nu(i,j)\, RRate(j,r_p,z,r)\, \rho_p \tag{3.5}$$

The energy balance for the solid also accounts for advection, dispersion and diffusion or conduction of heat. Since the reference state is pure compounds at standard conditions the heat of reaction is also added to the balance. The heat of reaction is calculated from the standard enthalpies of formation, ΔH_f^0.

$$\frac{1}{r_p}\frac{\partial}{\partial r_p}\left[r_p\, H_{r_p}^{adv}(r_p,z,r)\right] + \frac{\varepsilon_p}{r_p}\frac{\partial}{\partial r_p}\left[r_p\, H_{r_p}^{disp}(r_p,z,r)\right] + \frac{1}{r_p}\frac{\partial}{\partial r_p}\left[r_p\, H_{r_p}^{diff}(r_p,z,r)\right] + \sum_i\sum_j \nu(i,j)\, RRate(j,r_p,z,r)\, \rho_p\, \Delta H_f^0(i) = 0 \tag{3.6}$$

Pellet external mass and heat diffusion resistances are accounted for with the following boundary conditions, at the pellet surface, R_p. The heat and mass transfer film coefficients are denoted by k_f and h_f, respectively.

$$\varepsilon_p N_{r_p}^{diff}(i,r_p,z,r) = C_f\, k_f\, \left[x_p(i,r_p,z,r) - x_f(i,z,r)\right], \qquad r_p = R_p \tag{3.7}$$

$$H_{r_p}^{diff}(i,r_p,z,r) = h_f\, \left[T_s(i,r_p,z,r) - T_f(i,z,r)\right], \qquad r_p = R_p \tag{3.8}$$

Only the boundary conditions related to the bed heat balance equation (3.4) are presented, since they are the most important for this work. At bed centre line, a simple symmetry or adiabatic condition is imposed.

$$\frac{\partial}{\partial r} T_f(z,r) = 0, \qquad \forall z > 0, \qquad r = 0 \tag{3.9}$$

At the wall, the diffusive heat flux is equated to a heat flux from the wall using a bed-to-wall heat transfer coefficient, α_w.

$$H_r^{diff}(z,r) = \alpha_w\left[T_f(z,r) - T_{w,i}(z,r)\right], \qquad \forall z > 0, \qquad r = R \tag{3.10}$$

Finally, the diffusive heat flux is defined using an effective radial bed conductivity, $\lambda_{e,r}$.

$$H_r^{diff}(z,r) = -\lambda_{e,r}(z,r)\, \frac{\partial}{\partial r} T_f(z,r) \tag{3.11}$$

3.1.2 Steady-State Process Model Library – PML:SS

The gPROMS® Process Model Library for Steady State (PML:SS) provides modelling solutions for general process equipment such as distillation columns, heat exchangers or pumps and compressors. It also has control and signal libraries that allow the user to apply restrictions or design specifications on a flowsheeting environment.

Figure 3.3 portraits the main models used from PML:SS. The key model used was the *reactor_*conversion. The model allows the user to specify reaction stoichiometry and conversion, as well as pressure drop and thermal duties.

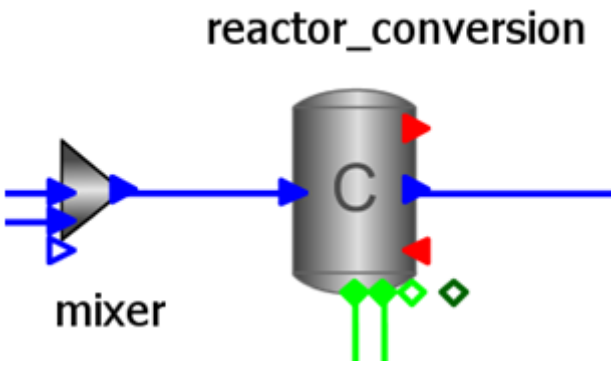

Figure 3.3 Main models from PML:SS.

3.1.3 Physical properties package

The physical properties package used was Multiflash® from Infochem Computed Services Ltd. Physical properties were predicted using GERG 2008 corresponding states model which is specific to natural gas applications.

3.2 Steam methane reformer

The SMR model main components are the reformer tube and the furnace or firebox. The reformer tube is modelled with a catalytic section model (two-dimensional bed with one-dimensional pellet) from the AML:FBCR. The heat from the furnace was modelled with two different approaches: the first one assigns a typical industrial temperature profile to the reformer tube wall; and the second uses the fired heater model developed during the course of this work. The customisations and specification options made to the AML:FBCR catalytic section are described under section 3.2.1 and the fired heater model is described under section 3.2.1.4.

A possible configuration for the SMR model is presented in Figure 3.4. There are two material stream sources, one for natural gas and another for steam; a junction (mixer); two catalytic reactor sections, one connected to a fired heater and the other working in adiabatic mode.

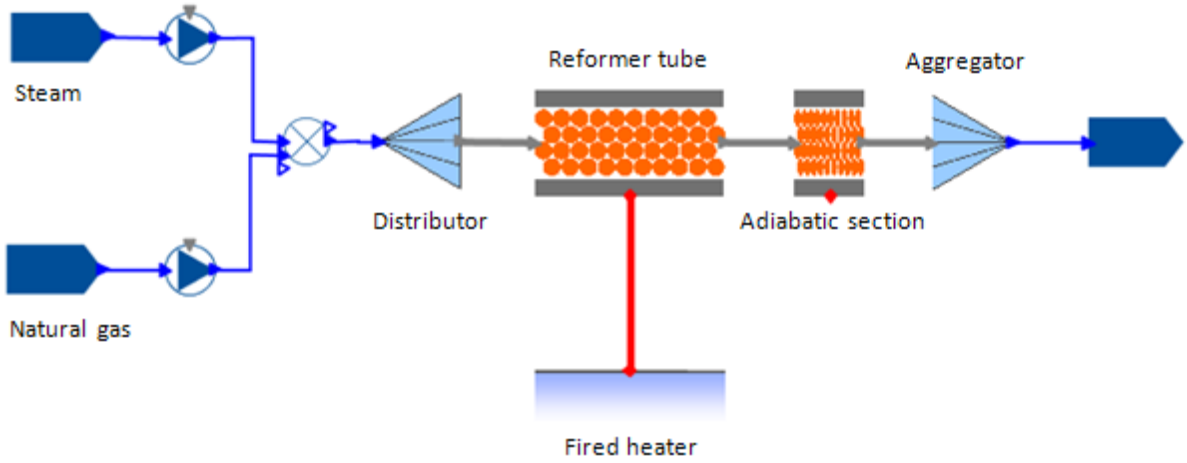

Figure 3.4 SMR model topology using a fired heater.

The model allows the user to specify the inlet S/C ratio. The model then calculates the inlet steam flowrate based on natural gas flowrate and composition.

Some key performance indicators are automatically calculated by the model:

- Outlet methane conversion;
- Outlet H_2/CO ratio;
- Outlet M module;
- Outlet molar composition in dry basis;
- Radial averaged fluid and solid temperatures;
- Maximum wall temperature;
- Overall Pressure drop.

3.2.1 Catalytic section

The AML:FBCR catalyst section model used here was the *Catalyst_Pellets_Section*. This section describes the specifications and some customisations made to some of the sub-models from Table 3.1. It also describes the options made for the methods used (see Table 3.2) and the rationale behind them.

3.2.1.1 Properties and parameters

This sub-model calculates diffusivity coefficients according to the equation proposed by Fuller, Schettler and Giddings [41].

The method needs atomic diffusion volumes for each component that are taken from table 11-1 in [42].

Table 3.3 Atomic diffusion volumes for Fuller's method [41].

	CH_4	H_2O	CO	CO_2	H_2	N_2	Units
V	25.14	12.23	18	26.9	6.12	18.5	-

3.2.1.2 Reaction kinetics

Reaction kinetics for steam reforming have been subjected extensive research since the 1960s and until now there are still doubts on the validity of the established reaction mechanisms under the wide range of conditions possible for steam reformers [34]. The difficulties arise from relatively fast and highly endothermic reactions which makes hard to obtain accurate measurements [32]. Although different kinetic equations have been proposed, Xu and Froment [9] established a Langmuir Hinshelwood based model in 1989 that has been extensively used since.

The kinetic model from [9] was implemented and considers three global reactions (3.12): steam reforming of methane to carbon monoxide, SR(I), and to carbon dioxide, SR(II) and water gas shift, WGS. As a simplification it was assumed the natural gas does not contain higher hydrocarbons so no reaction kinetics are needed for them.

$$\begin{aligned} CH_4 + H_2O &\rightleftarrows CO + 3H_2 && SR(I) \\ H_2O + CO_2 &\rightleftarrows CO + H_2 && WGS \\ CH_4 + 2H_2O &\rightleftarrows CO_2 + 4H_2 && SR(II) \end{aligned} \quad (3.12)$$

The three corresponding reaction rates, $RRate$, in [mol/kg_{cat} s] are presented below. The reaction rates are calculated using the partial pressures of each component i, p_i; the kinetic constant, k_j, and reaction equilibrium constant, K_j, of each reaction j; and the adsorption equilibrium constants, K_i, of each adsorbing component. The pressure unit used here is bar and the kinetic and equilibrium constants have the units correspondent to the respective pre-exponential factor in Table 3.4.

$$RRate(SR(I)) = \frac{\frac{k_{SR(I)}}{{p_{H_2}}^{2.5}}\left(p_{CH_4}\, {p_{H_2O}} - \frac{{p_{H_2}}^3\, p_{CO}}{K_{SR(I)}}\right)}{\left(1 + K_{CO}p_{CO} + K_{H_2}p_{H_2} + K_{CH_4}p_{CH_4} + K_{H_2O}p_{H_2O}/p_{H_2}\right)^2} \tag{3.13}$$

$$RRate(WGS) = \frac{\frac{k_{SR(I)}}{p_{H_2}}\left(p_{CO}\, {p_{H_2O}} - \frac{p_{H_2}\, p_{CO_2}}{K_{WGS}}\right)}{\left(1 + K_{CO}p_{CO} + K_{H_2}p_{H_2} + K_{CH_4}p_{CH_4} + K_{H_2O}p_{H_2O}/p_{H_2}\right)^2} \tag{3.14}$$

$$RRate(SR(II)) = \frac{\frac{k_{SR(I)}}{{p_{H_2}}^{3.5}}\left(p_{CH_4}\, {p_{H_2O}}^2 - \frac{{p_{H_2}}^4\, p_{CO_2}}{K_{SR(II)}}\right)}{\left(1 + K_{CO}p_{CO} + K_{H_2}p_{H_2} + K_{CH_4}p_{CH_4} + K_{H_2O}p_{H_2O}/p_{H_2}\right)^2} \tag{3.15}$$

Table 3.4 Steam reforming kinetic parameters for Arrhenius relation.

	Pre-exponential factor	Units	Activation energy	Units
$k_{SR(I)}$	$4.225 \cdot 10^{15}$	kmol $bar^{0.5}/kg_{cat}$ h	-240.1	kJ/mol
k_{WGS}	$1.995 \cdot 10^{6}$	kmol bar^{-1}/kg_{cat} h	-67.13	kJ/mol
$k_{SR(II)}$	$1.020 \cdot 10^{15}$	kmol $bar^{0.5}/kg_{cat}$ h	-243.9	kJ/mol
K_{CO}	$8.23 \cdot 10^{-5}$	bar^{-1}	70.65	kJ/mol
K_{H2}	$6.12 \cdot 10^{-9}$	bar^{-1}	82.9	kJ/mol
K_{CH4}	$6.65 \cdot 10^{-4}$	bar^{-1}	38.28	kJ/mol
K_{H2O}	$1.77 \cdot 10^{5}$	-	88.68	kJ/mol

Reaction kinetic parameters for equations (3.13) to (3.15) can be calculated from the data in Table 3.4 using the Arrhenius relation.

Equilibrium was calculated from equations 4-343 to 4-345 on page 4-32 of [43]:

$$\ln K_{eq}(j) = -\frac{\sum_i \nu(i,j)\, \Delta G_f^0(i)}{T} \tag{3.16}$$

Besides kinetic rate equations some key performance indicators were also calculated: the effectiveness factor, η, and the approach to equilibrium, App_{eq}:

$$\eta(j) = \int_0^{R_p} RRate(j, r_p)\, dr_p \Big/ RRate(j, R_p) \tag{3.17}$$

$$App_{eq}(j) = \frac{\prod_i {p_i}^{\nu(i,j)}}{K_{eq}(j)} \tag{3.18}$$

3.2.1.3 Bed properties

As it was suggested in Table 3.1 this model includes the correlations necessary to predict bed momentum, mass and heat transfer. This includes correlations for pressure drop (the Ergun equation) and for the radial heat transfer parameters used in equations (3.10) and (3.11): the bed-to-wall heat transfer coefficient, α_w, and the effective radial bed conductivity, $\lambda_{e,r}$.

A correlation to predict bed porosity was added to this model. The correlation of Reichelt and Blass [44] was used.

$$\varepsilon_b = 0.38 + 0.073\left[1 + \frac{\left(d_t/d_p - 2\right)^2}{\left(d_t/d_p\right)^2}\right] \tag{3.19}$$

Radial heat transfer parameters correlations were customised to the ones used in the original paper for the SMR case studied in section 4.1. These two parameters α_w and $\lambda_{e,r}$ have both a static and a dynamic contribution. The static contribution relates to heat transfer in the hypothetic situation of zero flow, while the dynamic contribution accounts for hydrodynamic effects.

$$\lambda_{e,r} = \lambda_{e,r}^{static} + \lambda_{e,r}^{dynamic} \tag{3.20}$$

$$\alpha_w = \alpha_w^{static} + \alpha_w^{dynamic} \tag{3.21}$$

These correlations were all used in [10] and can be found in [40].

$$\lambda_{e,r}^{static} = \lambda_f\left[\varepsilon_b\left(1 + 0.95\, d_p\left[0.227\frac{\left(\frac{T_s}{100}\right)^3}{1 + \frac{\varepsilon_b}{2(1-\varepsilon_b)}\frac{1-\xi_p}{\xi_p}}\right]\right) + 0.95\frac{(1-\varepsilon_b)}{1\Big/\left(\frac{1}{0.1} + \left[0.227\left(\frac{T_s}{100}\right)^3\Big/\frac{\xi_p}{2-\xi_p}\right]\frac{d_p}{\lambda_f}\right) + \frac{2}{3}\frac{\lambda_f}{\lambda_p}}\right] \tag{3.22}$$

$$\alpha_w^{static} = \frac{8.694}{{d_t}^{4/3}}\,\lambda_{e,r}^{static} \tag{3.23}$$

$$\lambda_{e,r}^{dynamic} = \lambda_{e,r}^{adj}\, 0.14\, Re\, Pr \tag{3.24}$$

$$\alpha_w^{dynamic} = \alpha_w^{adj}\, 0.444\, Re\, Pr\, \frac{\lambda_f}{d_p} \tag{3.25}$$

Please note the correlations for dynamic contributions include an adjustable parameter, $\lambda_{e,r}^{adj}$ and α_w^{adj}, that allows the user to estimate it and adjust the correlations to their own experimental data.

3.2.1.4 Methods

The methods chosen from Table 3.2 for this model are summarised in Table 3.5.

Table 3.5 SMR catalytic section specified methods.

Method	Options
Radial heat transfer media[6]	• Fluid only
Partial enthalpy	• Real mixture
Intra-particle diffusion	• Dusty-gas model
Extra-particle mass and heat transport	• Hougen (1961) correlations

The radial heat transfer was considered through fluid only since the major contribution to the radial heat transfer parameters α_w and $\lambda_{e,r}$ comes from fluid hydrodynamics; in other words, the major contribution in equations (3.20) and (3.21) is the dynamic contribution. Real mixture partial enthalpy calculations were used because syngas is a highly non-ideal system. Intra-particle diffusion is calculated using the Dusty-gas model as Knudsen diffusivity is used in [10]. Finally, solid-fluid heat and mass transport uses the correlations from Hougen (1961), the default option in AML:FBCR.

3.2.2 Fired heater

Detailed modelling of heat transfer from the firebox to the reformer tubes is a challenge. Modelling of radiative heat transfer needs intensive calculations, taking into account geometry view factors, gas emissivities and burner geometry. In this work a simplified approach to the furnace was used and radiation heat flux is calculated from a form of the Stefan-Boltzmann law. Equation (3.26) is used to calculate heat flux, q_w, or outer tube wall temperature, $T_{w,o}$, and applies two effective parameters: an effective emissivity, ξ_{eff}, and an effective temperature, T_{eff}.

$$q_w = \sigma\, \xi_{eff} \left({T_{w,o}}^4 - {T_{eff}}^4 \right) \tag{3.26}$$

This approach assumes radiation is the only form of heat transfer, neglecting convection contributions, which are typically not accounting for more than 5% of the heat transfer in firebox (due to linear dependence on the temperature difference, as opposed to the 4th power in radiative heat transfer driving force). The effective emissivity lumps geometry effects (number and location of burners, flame size, firebox size and number of burners); and emissivities from the different sources present (furnace, reformer tube, fluid and flame) [45].

3.3 Autothermal reformer

The ATR model main components are the combustion chamber and the catalyst fixed-bed section. The combustion chamber is modelled using a conversion reactor from PML:SS and some signal models to define reaction conversion extents. The catalytic section is modelled using an AML:FBCR model of a one-dimensional bed with one-dimensional pellet. The combustion chamber model is described under section 3.3.1 and the catalytic section model methods and customisations are explained under section 3.3.2.

[6] Only used for the two-dimensional bed model.

For this reformer model a one-dimensional bed, axially distributed without radial distribution, was considered because it is an adiabatic vessel and radial temperature profiles in the bed are negligible. In fact, a two-dimensional bed model, with both axial and radial distributions, was tested and predicted flat radial profiles. This is a simplification from the real situation where the flame in the combustion chamber induces a radial temperature profile along the reactor length. If a detailed combustion chamber model, considering the flame and radial temperature profiles was available, then a two-dimensional bed model should be used.

The ATR model topology is presented in Figure 3.5. There are two material stream sources, one for natural gas or pre-reformed gas and another for oxygen or air; the combustion chamber with the mixer, the conversion reactor and the signal blocks; a “gML to PML” connector; and the catalytic section.

The ATR model uses the combustion chamber model from PML:SS and the catalytic section model from AML:FBCR. To use these two libraries a “gML to PML” connector model is used to change the reference enthalpy state from pure elements (PML:SS) to compounds (AML:FBCR).

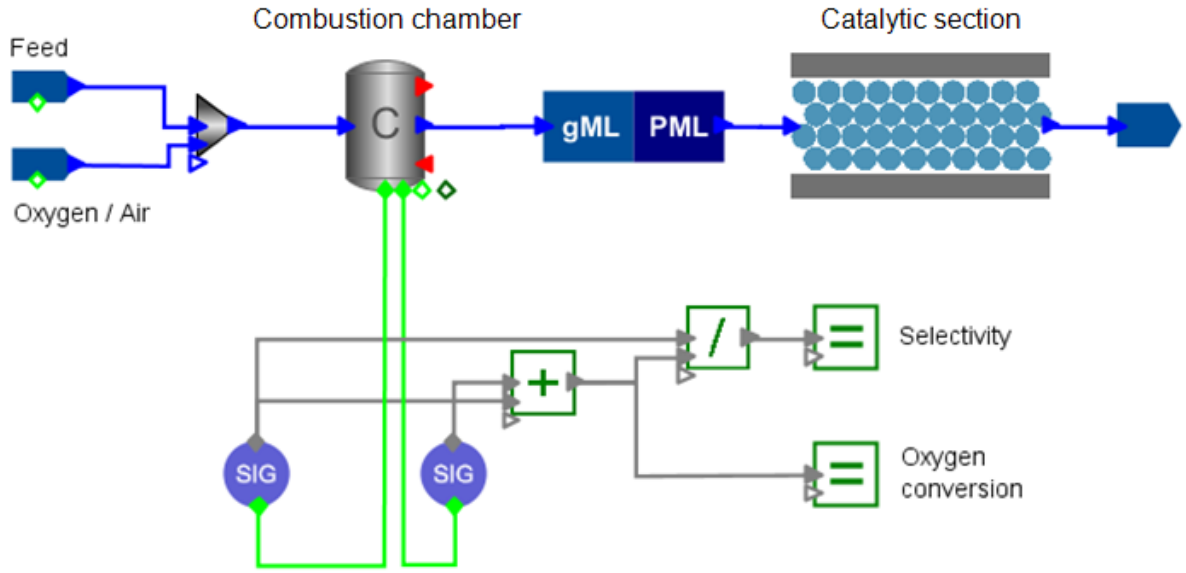

Figure 3.5 ATR model topology.

Some key performance indicators are automatically calculated by the model:

- Inlet O/C ratio;
- Outlet methane conversion;
- Outlet H_2/CO ratio;
- Outlet M module.

3.3.1 Combustion chamber

The combustion chamber is a key piece of equipment in an autothermal reformer. It acts as the heat source for the endothermic steam reforming reactions.

As it was explained under section 2.4.2 both combustion and SR reactions occur in homogenous phase, inside the combustion chamber. Given the complexity of the reaction schemes for radical combustion reactions and SR reactions, it is common to model these reactions in a simplified, one

molecular reaction (3.27). When the ATR acts as a secondary reformer, it receives a pre-reformed gas with a considerable hydrogen content, so hydrogen combustion was also considered [21].

$$CH_4 + 1.5\ O_2 \rightleftarrows CO + 2\ H_2O \tag{3.27}$$

$$H_2 + 0.5\ O_2 \rightleftarrows H_2O \tag{3.28}$$

The combustion chamber model has two main components: a mixer and the conversion reactor from PML:SS. It also uses some signal blocks to allow the user to quickly define the reaction conversion extents. This model topology is shown in Figure 3.6.

The conversion reactor model was set as an adiabatic reactor and the reactions stoichiometry was specified. Conversion extents use oxygen as the reference component and need to be defined for both reactions; this was accomplished using the signal blocks in Figure 3.6: the equal block for oxygen conversion defines complete oxygen conversion; and the equal block for reaction selectivity allows the user to choose between reactions (3.27) and (3.28), a value of 1.0 corresponds to reaction (3.27) only.

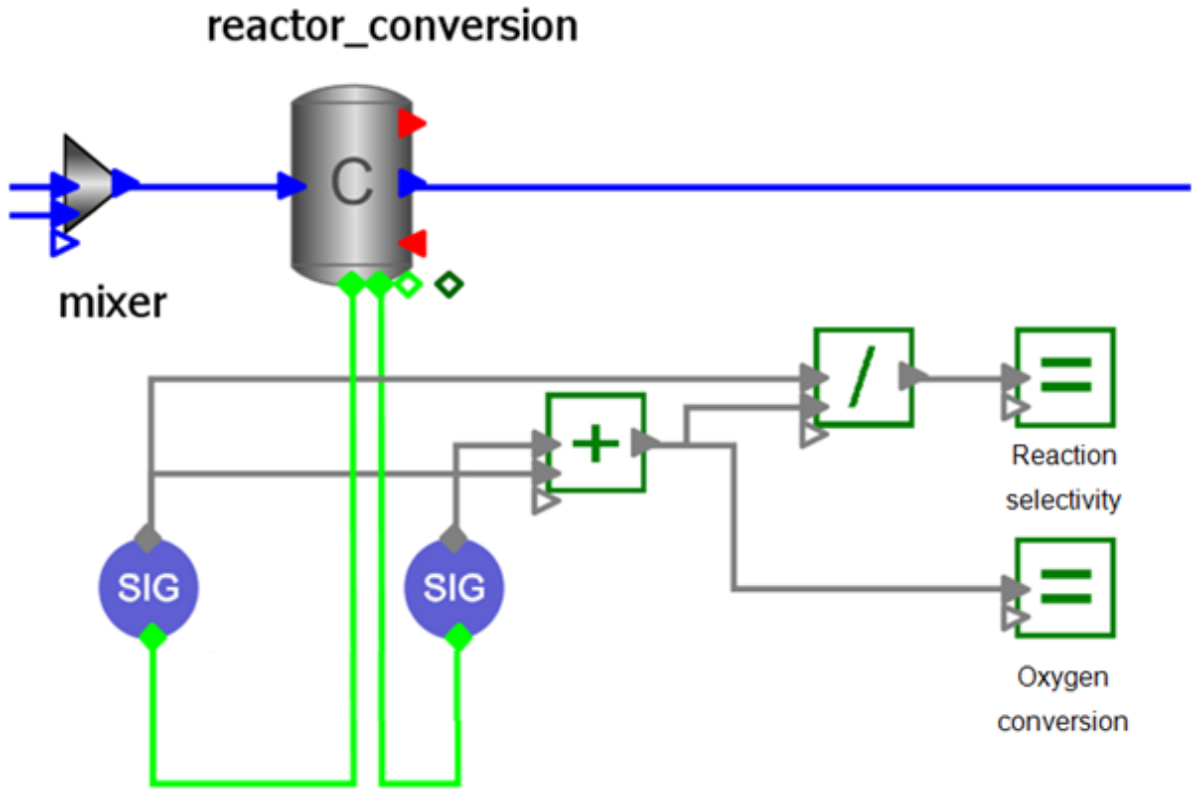

Figure 3.6 Combustion chamber model topology.

3.3.2 Catalyst section

The AML:FBCR model used for this catalyst section was the *Catalyst_Pellets_Section_1D_Adiabatic*. Although this catalyst section model is different from the one used for the SMR reactor the methods and sub-model customisations are essentially the same and were explained in more detail under section 3.2.1. This is not only because the models are very similar, but also because the phenomena taking place inside the catalyst section is the same.

The only relevant difference that comes from the absence of radial distribution and heat transfer is that there is no option for the radial heat transfer media.

4 Simulation Results

4.1 Steam Methane Reforming

The example used for this case study comes from the work by Xu and Froment and Plehiers and Froment [10,14] where an industrial side-fired steam reformer was modelled.

Initially, model configuration is presented with reactor dimensions, operating conditions and pellet model settings. The model was then tested by varying pressure, temperature and inlet S/C ratio. Finally, the case study results with fixed temperature profile and with heat flux calculated from a fired heater model are presented.

In [10], the reactor tube model consists of a one dimensional, axially distributed, bed model with fluid momentum, mass and energy balance; and of a one dimensional pellet model with mass balance to account for diffusion inside the particle. The firebox is modelled using a detailed zone method model.

4.1.1 Reactor configuration

Industrial reactor and catalyst characteristics are reported in Table 4.1 and inlet conditions in Table 4.2.

Table 4.1 SMR reactor and catalyst dimensions and properties.

Tube design		**units**	**reference**
Internal Radius	0.0508	m	[10]
Wall thickness	0.0153	m	[10]
Heated length	11.117	m	[10]
Total length	12	m	[10]
Wall conductivity	28.5	W/m/K	[13]
Wall emissivity	0.95		[26]
Catalyst ring			
Type	Ring-shaped		[10]
Outer diameter	17.3	mm	[10]
Inner diameter	8.4	mm	[10]
Height	10	mm	[10]
Thickness of active layer	2	mm	[10]
Bulk density	2355.2	kg/m3	[10]
Pellet porosity	0.59		[10][1]
Pellet tortuosity	3.54		[10]
Pellet mean pore radius	10.47	nm	[10][2]
Pellet conductivity	0.3489	W/m/K	[13]
Pellet emissivity	0.8		AML:FBCR default

[1] Calculated from table 1. in paper.

[2] Calculated from table 1. in paper, considering a 95% confidence interval from which the two largest pore size measurements were removed.

Table 4.2 SMR reactor inlet conditions.

	value	units
Temperature	793.15	K
Pressure	29.0	bar
Methane	5.168	kmol/h
Hydrogen to methane ratio	0.122	-
Carbon dioxide to methane ratio	0.056	-
Nitrogen to methane ratio	0.164	-
S/C ratio	3.358	-

Plant outlet conditions are reported in Table 4.3 and reformer wall temperature measurements in Table 4.4.

Table 4.3 SMR plant data outlet process and flue gas conditions.

	Plant data	units
Flue gas temperature	1273-1325	K
Process gas outlet temperature	1038	K
Catalyst bed outlet pressure	24.4	bar

Table 4.4 SMR plant data wall temperature measurements.

Z (m)	Outer wall temperature (K)
0.0	949.0
3.8	1055.2
6.0	1107.5
9.0	1150.1
11.1	1173.0
12.0	1019.4

4.1.1.1 Pellet settings

Catalyst pellets used in this reactor are in the form of egg-shell or coated catalyst rings so they will be modelled using one of the inert core pellet models available in AML:FBCR. There are two inert core pellet models: sphere and infinite cylinder. The choice fell upon the cylindrical pellet since its sphericity[3] is around 0.61.

The approach developed to define the correct pellet settings for non-ideal (non-spherical and non-cylindrical) shapes using a 1D geometry model was the following:

1. Conserve total amount of catalyst available for reaction, by conserving particle A/V ratio;
2. Conserve diffusion path by conserving layer thickness;
3. Conserve total mass of active catalyst (active layer) by correcting pellet density.

[3] Sphericity of a particle is defined as the ratio of the area of a volume-equivalent-sphere to the area of the particle.

This approach results in the following relations to calculate the model input variables.

$$r_p = \frac{2\,V^{real}}{A^{real}} \tag{4.1}$$

$$r_i = r_p - \delta \tag{4.2}$$

$$\frac{\rho_p^{corr}}{\rho_p^{real}} = \frac{(V_{ac}^{real}/V^{real})}{\frac{r_p{}^2 - r_i{}^2}{r_p{}^2}} \tag{4.3}$$

The table below summarises these pellet model settings.

Table 4.5 SMR Pellet settings.

	value	units
Pellet model	Cylindrical pellet with inert core	
Radius	3.080	mm
Inner radius	1.080	mm
Density correction	1.071	-
Pellet shape	Non-ideal shape	-
Area-to-volume equivalent diameter	9.24	mm
Volume equivalent diameter	15.08	mm
Area equivalent diameter	19.27	mm

4.1.1.2 Numerics

AML:FBCR library models make use of the finite difference method to solve differential equations. In finite difference method a distribution domain is divided into N elements and N-1 grid points, or nodes, need to be defined. There are four options to define those grid points:

- Uniform grid – no extra information needs to be provided;
- Logarithmic transformation – places more nodes towards the beginning of the domain and a transformation parameter needs to be provided;
- Exponential transformation – places more nodes towards the end of the domain and a transformation parameter needs to be provided;
- User defined grid – all N-1 nodes need to be provided.

The model used has three different distribution domains:

- Bed axial domain;
- Bed radial domain;
- Pellet radial domain.

These grid settings were defined by trial and error: key performance indicators (KPI) and relevant profiles (axial and radial temperature profiles and pellet radial composition profiles) where monitored, while the number of elements was increased and their position (or grid transformation) was changed. The final grid settings chosen reflected only minor changes to those KPIs and profiles and can be found in Table 4.6 and Table 4.7.

Table 4.6 SMR Distributed domain grid settings.

Domain	Bed axial (catalyst section)	Bed axial (adiabatic section)	Bed radial	Pellet radial
Number of elements	16 (15) [4]	3	8	12
Grid transformation	User-defined (Logarithmic)[4]	Logarithmic	Exponential	User-defined
Transformation parameter	(10.0) [4]	10.0	1.0	-

Table 4.7 SMR Pellet radial user-specified grid points.

Pellet radial grid points										
0.200	0.400	0.700	0.861	0.908	0.935	0.954	0.969	0.981	0.991	0.996

The non-uniform grids chosen reflect the system's non-uniform behaviour: steep temperature drop at the beginning of the bed axial domain (inlet) - see Figure 4.8; high heat fluxes and temperature gradients near the end of the bed radial domain (wall) – see Figure 4.9; and very high gradients at the end of the pellet radial domain (pellet surface) – see Figure 4.11.

4.1.2 Thermodynamic results

Thermodynamic equilibrium was predicted using this reactor model. These results show the influence of temperature, pressure and inlet S/C ratio on outlet composition and methane conversion.

The figures below clearly depict equilibrium constraints on steam reforming reactors. They are important restrictions which need to be taken into account in reactor design and operation, and explain why steam reforming reactors need to operate at such high temperature and pressure conditions.

The equilibrium profiles in the figures below were predicted by increasing the fired heater temperature at different pressures (20 and 30 bar), and S/C ratios (1.0, 2.0 and 4.0); the reaction kinetic constants were increased by a factor of 10 to ensure the reaction mixture attained equilibrium.

Figure 4.1 and Figure 4.2 show the influence of temperature and pressure on SR equilibrium composition.

[4] This domain's user-defined grid corresponds to the 15 element logarithm transform with one extra element located at 0.008.

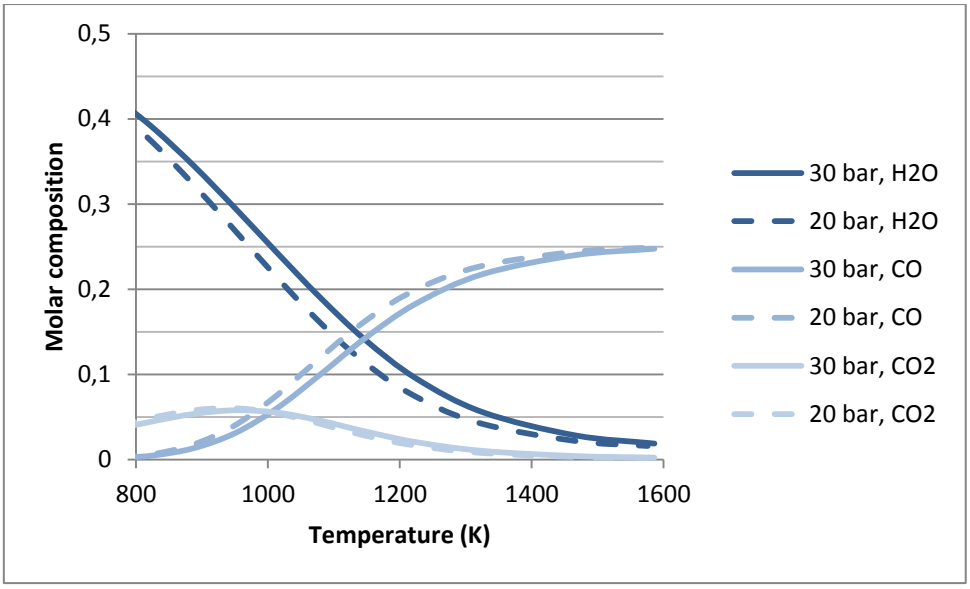

Figure 4.1 Equilibrium composition as a function of temperature at S/C ratio of 1 and different pressures (20 and 30 bar) – (1 of 2).

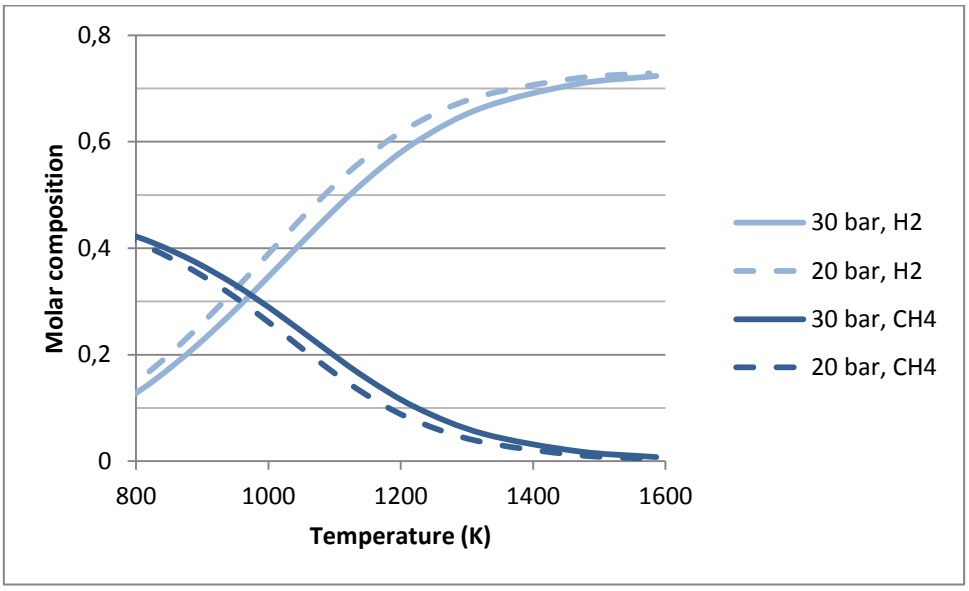

Figure 4.2 Equilibrium composition as a function of temperature at S/C ratio of 1 and different pressures (20 and 30 bar) – (2 of 2).

The two main reactions in steam reforming are opposite in thermal nature: WGS is exothermic whilst SR is endothermic. This means lower temperatures favour WGS reaction and higher temperatures favour SR reaction. In Figure 4.1 this behaviour is evident where CO_2, produced only from WGS, shows a maximum around 950 K and then disappears at higher temperatures; higher H_2 and CO compositions are also a consequence.

Figure 4.3 shows the influence of temperature at different pressures (20 and 30 bar) and at different S/C ratios (1.0, 2.0 and 4.0).

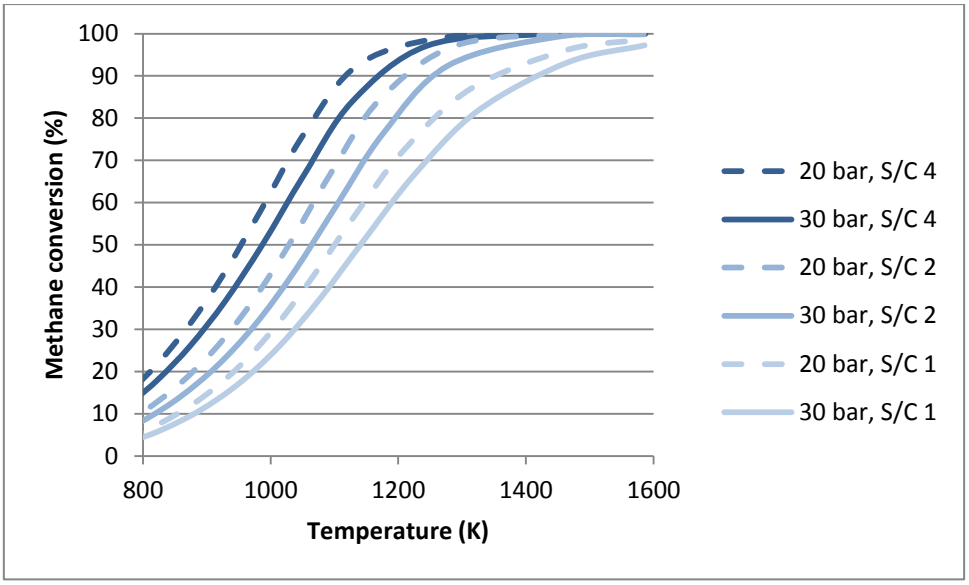

Figure 4.3 Methane equilibrium conversion as a function of temperature at different pressures (20 and 30 bar) and at different S/C ratios (1, 2 and 4).

Industrial operation often requires high pressure – due to downstream equipment operating conditions (e.g. ammonia production) or techno-economic equipment size restrictions – and low S/C ratio – as it allows higher thermal efficiency. But the SR reaction on the other hand, according to Le Chatelier's principle, is favoured by low pressures and high S/C ratios, as can be seen in Figure 4.3.

4.1.3 Case I: Fixed temperature profile

The industrial reactor example was taken from the work in [10,14]. Here, the reactor was modelled using the SMR model described in section 3.2, by applying a fixed polynomial temperature profile from the plant data in Table 4.4. This approach was also used recently in [13].

4.1.3.1 Matching plant outlet conditions

In this section the reactor model will be fine-tuned to try and match plant outlet temperature and pressure conditions, from Table 4.3.

The heat transfer from the furnace is the key limiting factor for SMR reactors. The radial heat transfer depends on the parameters α_w and $\lambda_{e,r}$ (see equations (3.10) and (3.11)), predicted by the correlations from section 3.2.1.3. These are effective parameters that depend on fluid properties, and on bed properties like bed porosity, catalyst size, shape and material, and their influence on a particular reactor is difficult to measure. For these reasons the radial heat transfer parameters were adjusted to the reported plant measurements.

Since the provided plant data doesn't allow distinction between fluid temperatures at different radial positions, and between fluid and wall temperature, the adjustable factors for both coefficients ($\lambda_{e,r}^{adj}$ and α_w^{adj}) were taken as equal; this way, only one adjustable factor for radial heat transfer was adjusted: α^{adj}. In fact, [10] shows fluid bulk and inner wall temperature profiles, but these are simulation results – not plant data – and will be compared to this work's predictions further ahead.

An initial sensitivity analysis to the radial heat transfer parameters was performed by reducing them from 100% to 25% (α^{adj} from 1.00 to 0.25). Its influence on temperature profiles, and on outlet temperature and pressure is shown in Figure 4.4 and Figure 4.5, respectively.

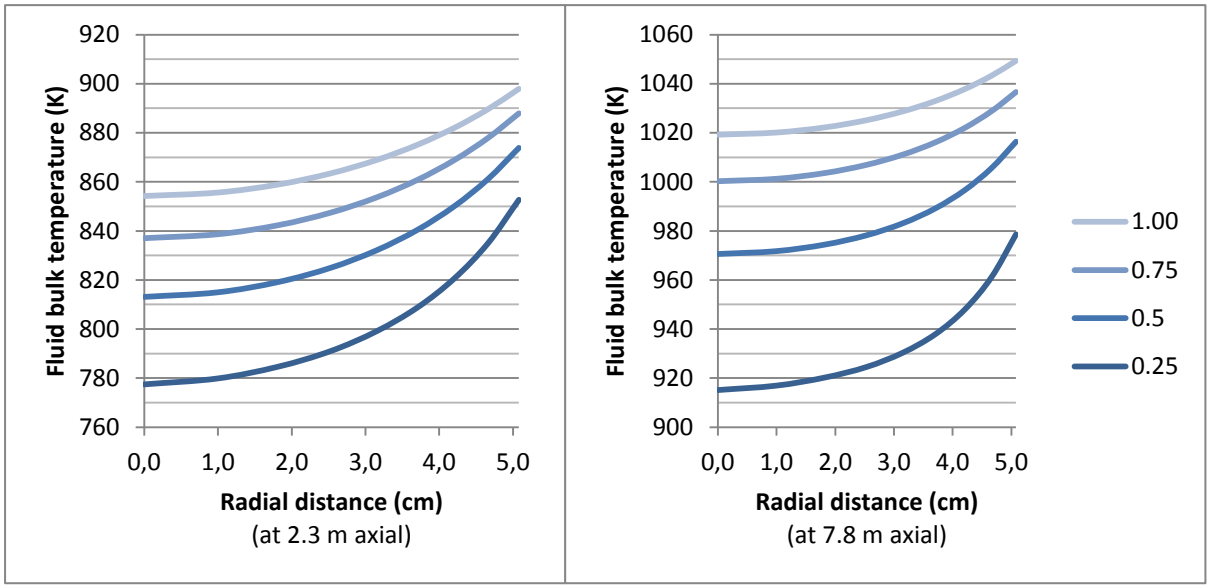

Figure 4.4 Sensitivity analysis to heat transfer coefficients ($0.25<\alpha^{adj}<1.0$): radial temperature profile.

Figure 4.4 shows the influence of the heat transfer coefficients on radial temperature profiles. Even without increasing this resistance to radial heat transfer the radial profile already shows a large temperature gap, around 50 K at 2.3 m reactor length and still around 30 K at 7.8 m reactor length, and this happens over only a 5 cm distance. This is a direct consequence of the high endothermic nature of this reaction system and is also reflected in the simulation profiles from [10,14].

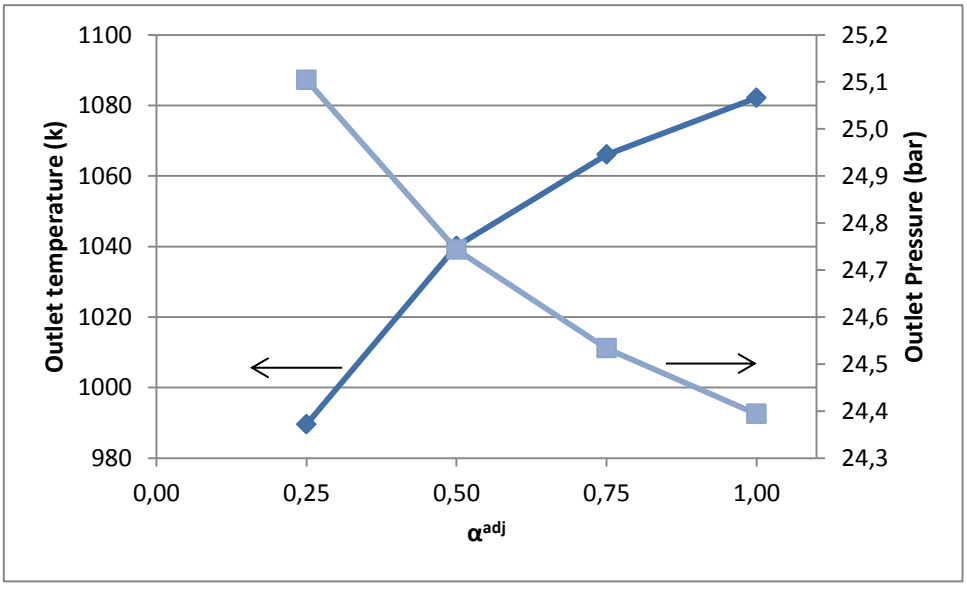

Figure 4.5 Sensitivity analysis to heat transfer coefficients: outlet temperature and pressure.

Figure 4.5 indicates it is possible to match outlet temperature by reducing the heat transfer coefficients down to 50%. This adjustment is yet insufficient, since it cannot match both outlet temperature and pressure, another parameter, related to pressure drop, needs to be adjusted to match outlet pressure.

The difference in predicted and industrial outlet pressures could arise from inlet and outlet manifold or distributor systems pressure drop. Although this is a valid cause for the differences, this type of pressure drop should be minimal to ensure even distribution between tubes, and so the major pressure drop was considered to be caused by the bed resistance.

A key property on fixed-bed reactor design is bed porosity. It affects not only pressure drop as well as heat and mass transfer and total mass of catalyst in the reactor – or total reactor volume. It is difficult to measure and it can change with time due to deposits, sintering or even breakage.

In this case the model is using a correlation to predict bed porosity (3.19). It was studied for spherical particles and takes into account the wall effect from the relation d_p/d_t which is considerably high in this case. Predicted values from this correlation may vary significantly from the real ones since the particles used are rings, not spheres, and because the wall effect correction varies also with the choice of equivalent diameter.

Since bed porosity significantly affects reactor performance, it was adjusted along with the previously analysed heat transfer adjustable factor to match outlet temperature and pressure; the results are given in Table 4.8.

Table 4.8 Comparison before and after matching model to outlet conditions.

	Initial	Final	Plant data
α^{adj}	1	0.489	-
ε_b	0.489	0.480	-
Outlet T (K)	1082.1	1038.0	1038.0
Outlet P (bar)	24.4	24.4	24.4

4.1.3.2 Simulation results

Finally, simulation results are compared against the industrial data and other simulation results presented in [9,14].

Table 4.9 SMR simulation results comparison with original paper.

	Plant data	Present work	Plehiers, 89
Conversion[5]	64.5% - 70.2%	61.6%	47.0%
H_2/CO	7.41 - 7.98	7.88	7.86
Outlet T (K)	1038.0	1038.0	1033.0
Outlet P (bar)	24.4	24.4	25.6

Simulation results in Table 4.9 reveal the model developed in this work has better agreement with plant data than the one used by the original authors. It is also interesting to see that although predicted conversion is closer to plant data, there is still a small gap between these two.

The difference in predicted conversion could be due to reactor operation away from equilibrium, but Figure 4.10 shows reaction rates close to zero at reactor outlet, so the reaction mixture at the outlet of the adiabatic section must be close to equilibrium. In fact, according to Figure 4.3, in order to achieve

[5] Conversion values reported here were calculated from a mass balance to the reported results in [14].

conversions like the ones reported in plant data the reactor would need to operate at lower outlet pressure, higher inlet S/C ratio or higher outlet temperature.

According to these results the model suggests plant data conversion is better than equilibrium conversion, which is impossible. It could be the thermodynamic model used in this work is not suitable but it was specifically designed for this type of mixture and its predictions agree with literature (see Figure 3 in [46]); moreover Peng-Robinson and Redlich-Kwong Soave equations of state were tested and only minor deviations from the latter were detected. It is also possible the assumption of ideal gas for reaction rates and reaction equilibrium is not valid and that vapour fugacity rather than vapour concentration should be used. Yet another possibility is these differences arise from inaccurate plant measurements, as a result of temperature or pressure drops in the reactor outlet system or from non-uniform operation between different catalyst tubes inside the reformer. With the limited information about these plant measurements, I consider this last possibility to be the strongest cause for this problem; more information like variance of the measurements would be helpful for this diagnostic.

Outlet molar composition in Figure 4.6 reflects the deviations in conversion while outlet molar composition on dry basis in Figure 4.7 reflects the agreement in H_2/CO ratio.

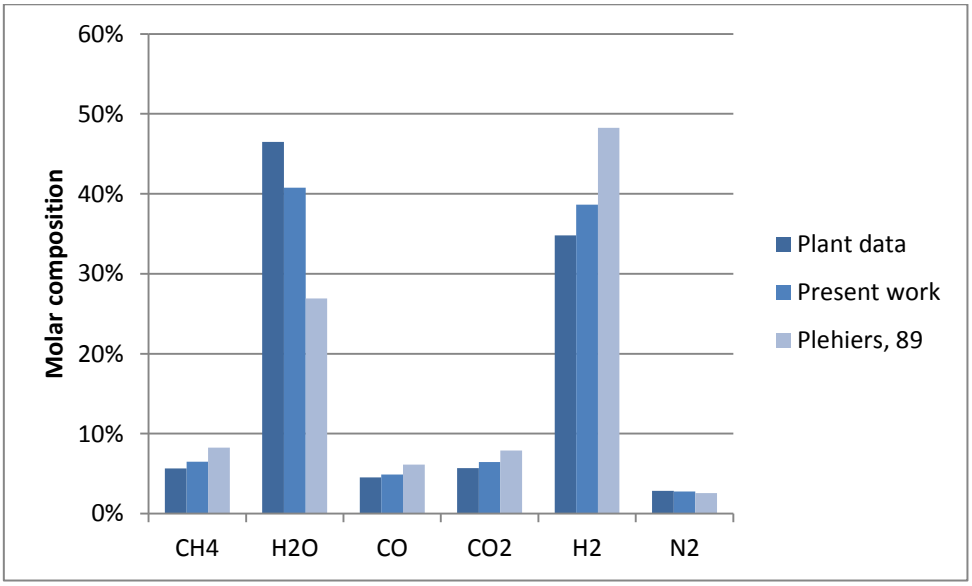

Figure 4.6 SMR Case I outlet molar compositions (plant data uses average values).

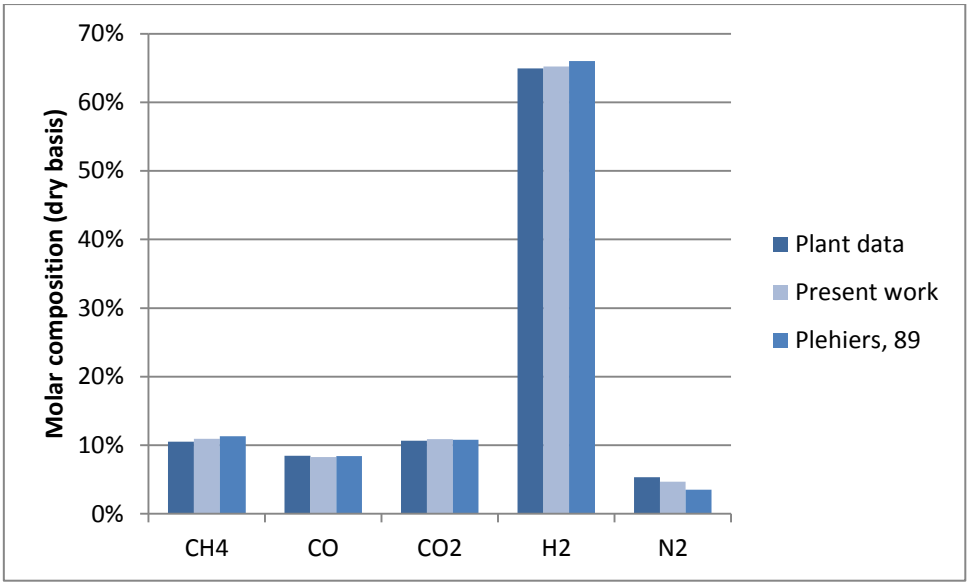

Figure 4.7 SMR Case I outlet molar dry compositions (plant data uses average values).

Figure 4.8 shows simulated temperature profiles and also includes predicted fluid temperature from the original work.

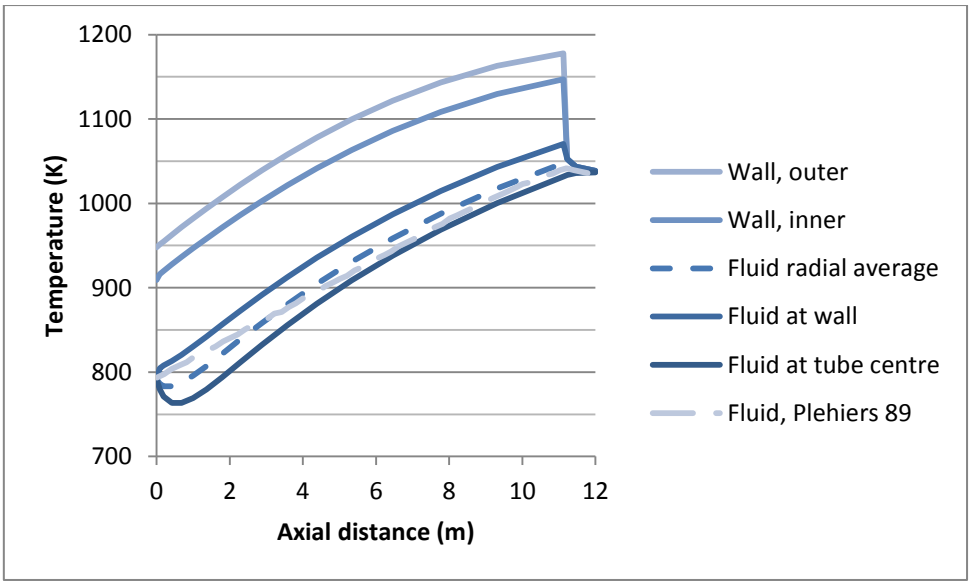

Figure 4.8 SMR Case I axial temperature profiles.

The model used in this work calculates a radial average fluid temperature which can be compared to the one dimensional temperature profile from the original paper. The two profiles are close to each other and are similar in trend with exception of the entry region, the first 2 meters of catalyst bed. In this region a temperature drop, of around 30 K at tube centre, is observed in the two dimensional model, which is due to the strongly endothermic reactions in SR and isn't detectable in Plehiers' profile.

Radial temperature profiles also give a clear proof of how energy demanding and endothermic this process is. Xu's model predicts a maximum temperature difference between wall and fluid of almost 200 K while the present simulation predicts a value of 150 K, considering fluid radial average temperature, or of 120 K, considering fluid temperature at the wall.

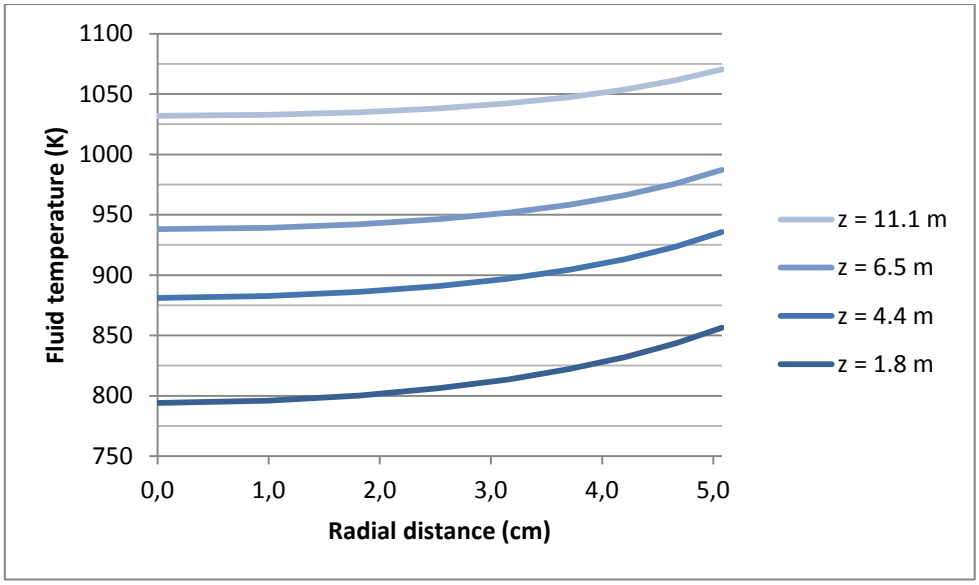

Figure 4.9 SMR Case I radial fluid temperature profiles.

These two figures, Figure 4.8 and Figure 4.9, show a steady temperature difference across the bed around 50 K. Validity of this value could be placed in question since there wasn't plant data available to correctly estimate heat transfer coefficients correction factors, and these coefficients are being reduced to 50%, but this difference was already present in Figure 4.4 with the original correlation prediction (α^{adj} of 1.0); moreover, literature and previous simulation works also exhibit such high temperature differences.

Reaction rate axial profiles from Figure 4.10 show very similar trend to the ones in Figure 4 from [10]; the only difference is their magnitude, these ones have a larger magnitude because they are calculated at the wall – where temperature is highest.

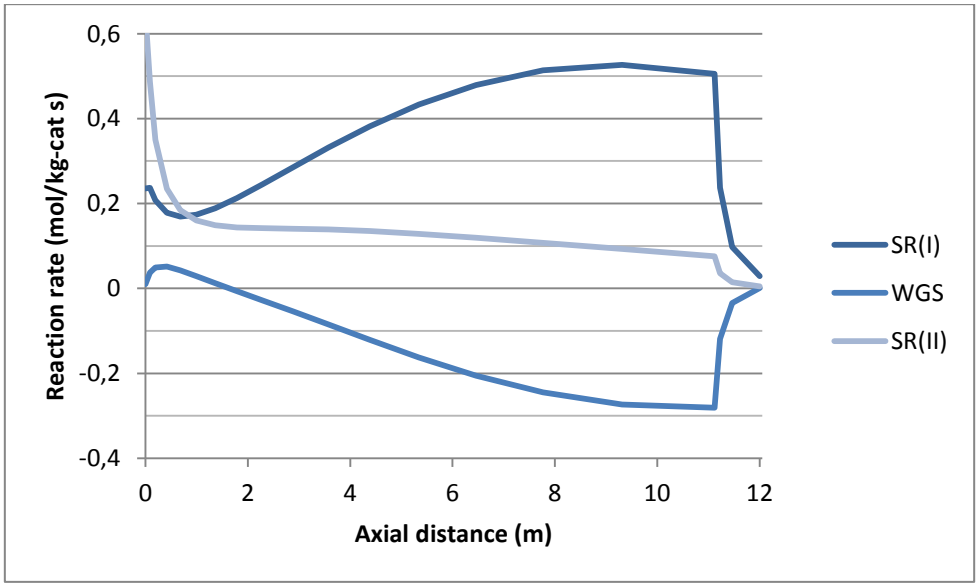

Figure 4.10 SMR Case I pellet surface reaction rates axial profile, at wall radial position.

Other key phenomena in steam reforming are pellet heat and mass transport limitations. Typically in steam reformers major restrictions to heat transfer are external limitations – 5-10 K temperature drop in the gas film surrounding the particle – and to mass transport are internal limitations – reaction rates are severely restricted by pore diffusion reflecting very low effectiveness factors [32,33].

From the simulation results in Figure 4.11, it can be seen although catalyst pellets' active layer is 2 mm thick, the reaction occurs almost only at the surface particularly on the outer 0.3 mm, which means only 15% of the active layer is used. This means reaction rates are diffusion controlled even though diffusion rates could be expected to be high in presence of small gaseous molecules, like hydrogen, and at high temperatures.

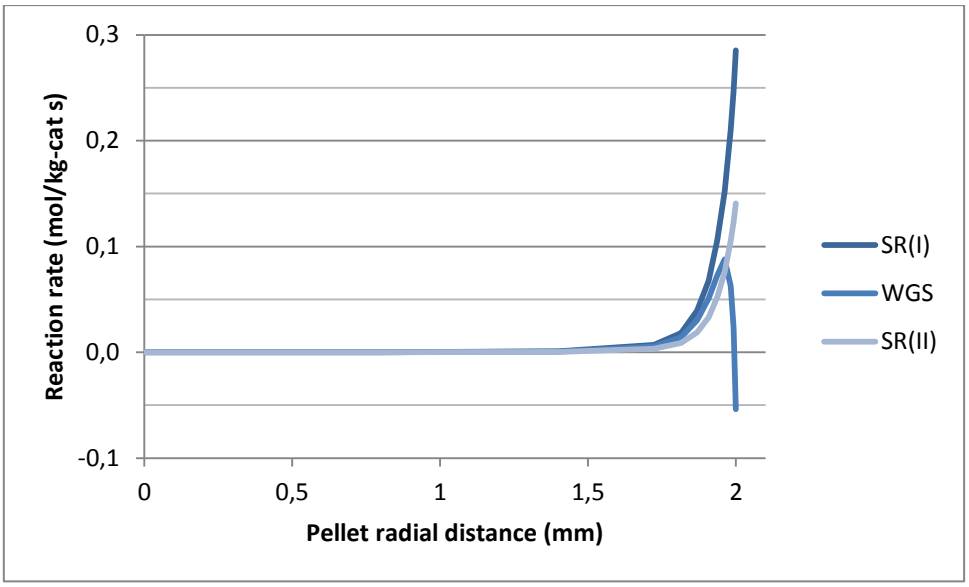

Figure 4.11 SMR Case I reaction rates radial pellet profile, at radial wall position and 2.9 m axial position.

The effectiveness factors presented in Figure 4.12 are in agreement with the general literature that says they are under 10% [32,33]; only WGS presents higher values in the beginning of the reactor. There is a discontinuity in WGS effectiveness factor, around 2 m, this happens when WGS reaction starts to change direction (from positive to negative) at pellet surface (see Figure 4.11); it finally changes back from negative to positive, around 9 m, where global WGS reaction rate inside the particle also reverses direction (becomes negative).

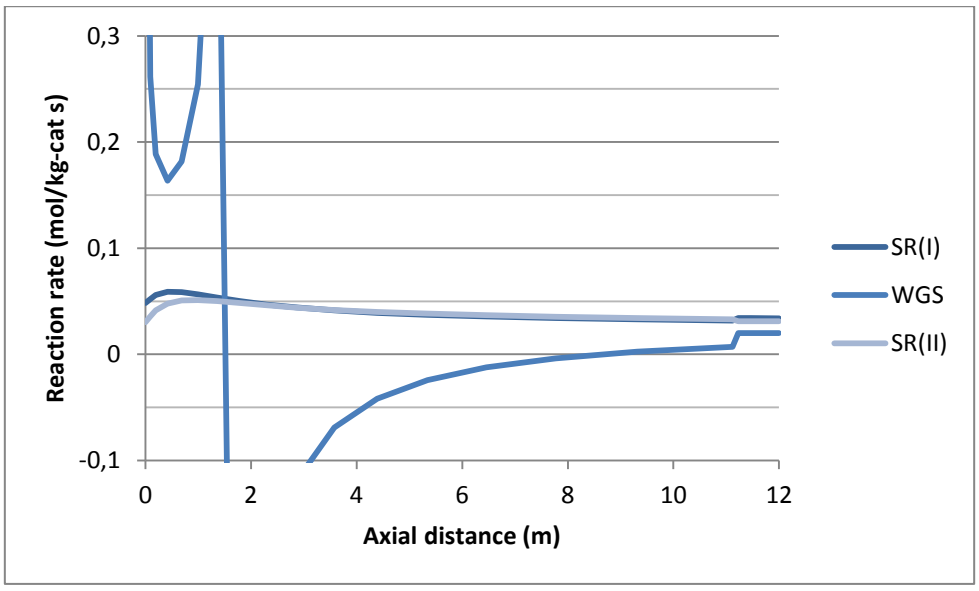

Figure 4.12 SMR Case I effectiveness factors axial profile, at wall radial position.

These two figures, Figure 4.11 and Figure 4.12, show it is essential to consider multi-component diffusion inside the pellet medium, when modelling steam reforming reactors, rather than using pseudo-homogeneous models with fixed effectiveness factors.

External heat transfer limitations are depicted in Figure 4.13. This heat transfer resistance is highest at wall radial position where it reveals a temperature drop of 9-10 K over the gas film surrounding the particle, values which agree with literature information referred to above.

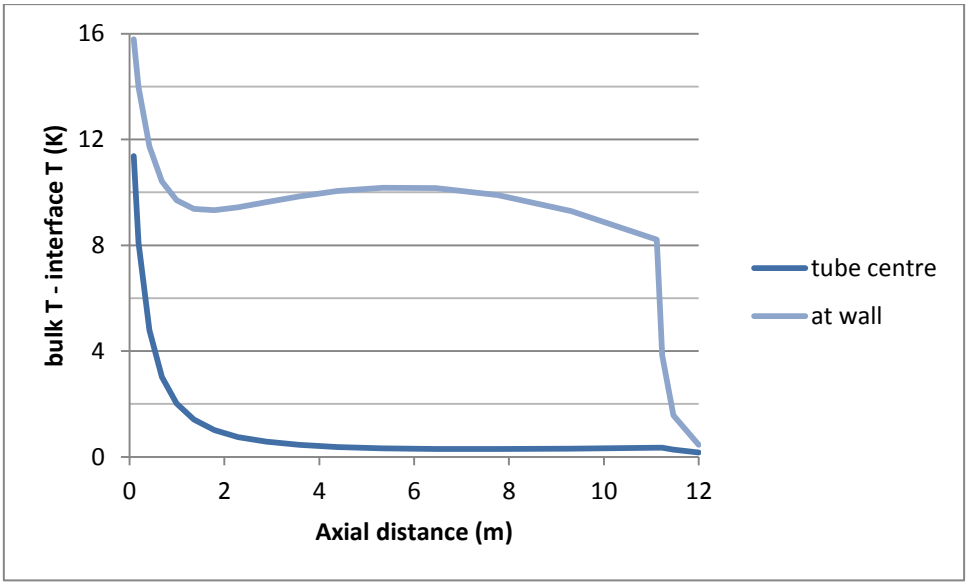

Figure 4.13 SMR Case I external heat transfer limitations.

The model used by Xu and Froment assumed concentration gradients occurred only on 0.08 mm of the total 2 mm active layer and modelled only those 4% of total active layer. While it is true that reaction does not occur on most of the active layer, 4% seems to be too restrictive. They also neglect any type of external limitations to heat and mass transport, but here it was demonstrated that, according to more recent literature, they are not negligible.

4.1.4 Case II: Fired heater

Here the same SMR industrial case used for Case I was modelled using the fired heater model described in section 3.3.1. The objective is to attempt to provide to the reactor model a calculated heat flux rather than a fixed temperature.

The fired heater model uses as inputs effective temperature and emissivity. Their values were determined by trading off their specification with outlet temperature and pressure (in other words the variables to be determined were used as output while outlet temperature and pressure as input to the model), the results are presented in Table 4.10.

Table 4.10 SMR Case II: Fired heater predicted parameters.

	model prediction
Effective emissivity	0.13
Effective temperature (K)	1741.4

The value for temperature represents an effective temperature between the adiabatic flame temperature (~2223 K)[6] and flue gas temperature (1273-1325 K) reflecting heat transfer contributions from walls, flame and flue gas.

Regarding the value for effective emissivity, one must recall this is a simplified model where geometry influence is taken into account in this effective emissivity, which is why the value falls outside the usual emissivity values (0.6-0.95). Taking as an example the equation used for calculating furnace heat fluxes in [47], effective emissivity relates to an intricate relation between areas and emissivities with a value of 0.23 for flue gas radiation contribution.

Figure 4.14 includes a sample profile with effective temperature and emissivity values of 1300 K and 0.75, respectively. It can be seen this profile with typical gas temperature and emissivity does not match the plant profile.

The predicted outer tube wall profile in Figure 4.14 reasonably agrees with plant temperature measurements, even though they weren't used to estimate any of fired heater model parameters. It is also seen that the sample profile with typical gas temperature and emissivity, although matching reactor outlet temperature, does not represent the measured temperature profile.

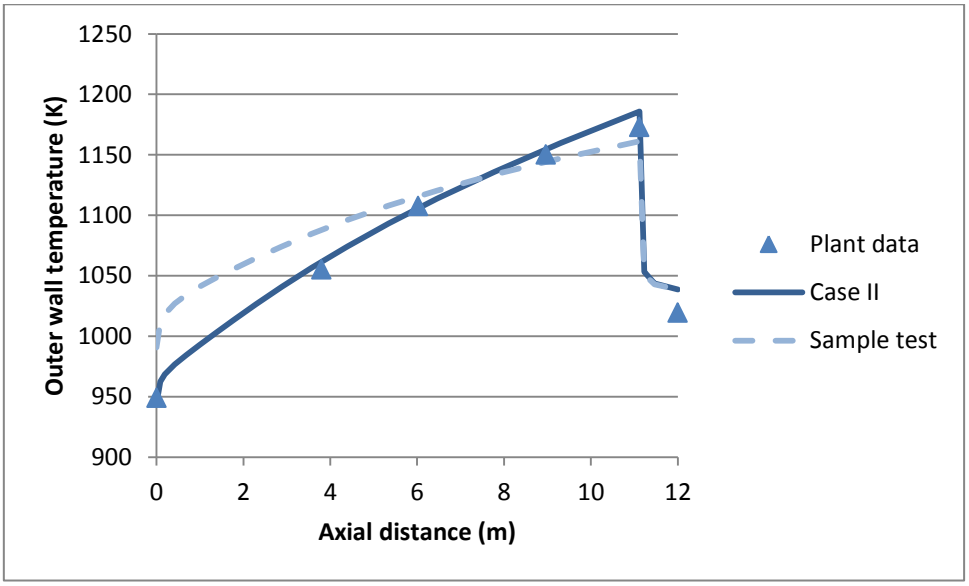

Figure 4.14 SMR Case II Outer wall temperature profile, results, plant data and a sample profile with 1300 K effective temperature and 0.75 effective emissivity.

Heat flux shape and order of magnitude from Case II in Figure 4.15 resemble the results for a side-fired reformer as in figure 7 of [48].

[6] Value for methane/air adiabatic flame temperature, the major component of the fuel used in [14].

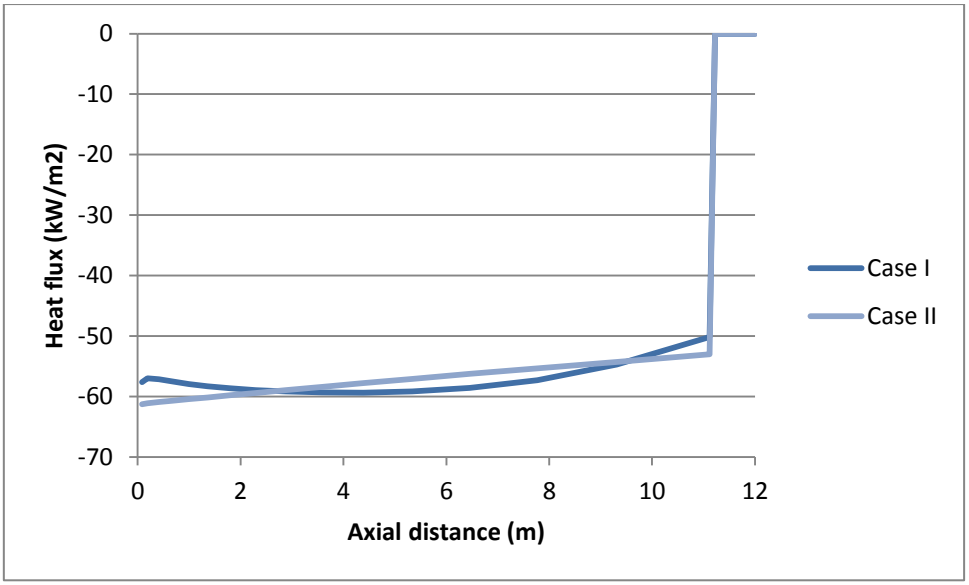

Figure 4.15 SMR heat flux profile comparison between Case I and II.

The simplified furnace model used in this case study is able to predict reasonable temperature and heat flux profiles for this industrial side-fired reformer. It does not replace the need for a more detailed furnace model, but, in light of these results, it will be used for optimisation.

4.2 Autothermal Reforming

The example used for this case study comes from the work by Al-Dhfeery et. al. [20] where an industrial secondary reformer was modelled.

Initially model configuration is presented with reactor dimensions, operating conditions and pellet model settings. The model was then tested by varying combustion reaction selectivity. Finally, the case study results are presented.

In [20], their reactor model consists of a global mass and energy balance for the combustion zone, and of a one dimensional, axially distributed, bed model with fluid momentum, mass and energy balance with reaction rates calculated from effectiveness factors and Thiele modulus.

4.2.1 Reactor configuration

Reactor and catalyst characteristics are reported in Table 4.11, inlet conditions in Table 4.12 and plant data in Table 4.13.

Table 4.11 ATR reactor and catalyst dimensions and properties.

Catalyst section design[7]		units	reference
Internal Radius	1.725	m	[20]
Wall thickness	0.440	m	[20]
Height	2.781	m	[20]
Catalyst ring			
Type	Ring-shaped		[20]
Outer diameter	19	mm	[20]
Inner diameter	9	mm	[20]
Height	19	mm	[20]
Bulk density	2248.7	kg/m3	[20][8]
Pellet porosity	0.4		AML:FBCR default
Pellet tortuosity	1.732		AML:FBCR default
Pellet mean pore radius	20.0	nm	AML:FBCR default

Table 4.12 ATR reactor inlet conditions.

Process gas	value	units
Temperature	1068.15	K
Pressure	32.0	bar
Methane	426.0	kmol/h
Hydrogen to methane ratio	6.88	-
Carbon dioxide to methane ratio	1.26	-
Carbon monoxide to methane ratio	0.947	
Nitrogen to methane ratio[9]	0.038	-
S/C ratio	8.65	-
Oxygen rich air		
Temperature	823.15	K
Pressure	32.0	bar
O/C ratio	0.857	-
Nitrogen to oxygen ratio	3.76	-
Steam to oxygen ratio	0.031	-
Carbon dioxide to oxygen ratio	0.001	-

[7] Inert catalyst sections of the reactor were neglected for this study.

[8] Calculated from pellet filling density.

[9] Argon was included as nitrogen.

Table 4.13 ATR reactor plant data.

		units
Outlet temperature	1242.15	K
Outlet pressure	31.57	bar
Conversion	95.6%	
H_2/CO	4.39	
H_2/N_2	2.51	
$(H_2+CO)/N_2$	3.08	

4.2.1.1 Pellet settings

Catalyst pellets used in this reactor are whole pellets so they were modelled using one of the standard pellet models without inert core available in AML:FBCR library. There are three possible pellet models: sphere, infinite cylinder or infinite hollow cylinder.

The approach followed to define the correct pellet settings came from AML:FBCR pellet geometry settings guideline [49]:

1. Conserve total available amount of catalyst available for reaction, by conserving particle A/V ratio;
2. Choose pellet geometry to best represent the real diffusion path.

From the catalyst dimensions in Table 4.11, it can be seen the real diffusion path will always be lower than 2.5 mm (half the thickness of the ring). Bearing this in mind both cylindrical pellet dimensions were calculated; formula for infinite cylinder is equation (4.1) and for hollow pellet is equation (2.5) where one of the radius needs to be assumed.

$$\frac{A^{real}}{V^{real}} = \frac{2(r_p + r_i)}{{r_p}^2 - {r_i}^2} \tag{4.4}$$

Table 4.14 ATR pellet models diffusion path.

				units
Pellet model	Cylindrical pellet	Cylindrical hollow pellet	Real pellet	
Radius	3.96	8.50	-	mm
Inner radius	0.00	4.54	-	mm
Diffusion path	3.96	1.98	< 2.5	mm

The pellet model chosen was cylindrical hollow pellet to best represent the real diffusion path. Table 4.15 summarises pellets settings for this case.

Table 4.15 ATR pellet model settings.

		units
Pellet model	Cylindrical hollow pellet	
Radius	8.500	mm
Inner radius	4.542	mm
Pellet shape	Non-ideal shape	-
Area-to-volume equivalent diameter	11.88	mm
Volume equivalent diameter	19.98	mm
Area equivalent diameter	25.92	mm

4.2.1.2 Numerics

The model used for ATR has two different distribution domains:

- Bed axial domain;
- Pellet radial domain.

The grid settings were chosen by a trial and error process similar to the one used for the SMR case study (see section 4.1.1.2), and are presented in Table 4.16 and Table 4.17.

Table 4.16 SMR Distributed domain grid settings.

Domain	**Bed axial (catalyst section)**	**Pellet radial**
Number of elements	16 (15) [10]	20
Grid transformation	User-defined (Logarithmic) [10]	User-defined
Transformation parameter	(10.0) [10]	-

Table 4.17 SMR Pellet radial user-specified grid points.

Pellet radial grid points									
0.004	0.009	0.019	0.031	0.046	0.065	0.092	0.139	0.300	0.500
0.700	0.861	0.908	0.935	0.954	0.969	0.981	0.991	0.996	

The non-uniform grids chosen reflect the system's non-uniform behaviour: higher gradients at the beginning of the axial domain (inlet) - see Figure 4.19; and very high gradients at the boundaries of the pellet radial domain (pellet surface) – see Figure 4.20.

4.2.2 Sensitivity analysis: Combustion chamber

The combustion chamber was modelled as a conversion reactor where oxygen is depleted. Since the reactor considered here is a secondary reformer, its feed contains methane and hydrogen, and a choice has to be made regarding selectivity of oxygen for methane partial combustion and hydrogen combustion.

[10] This domain's user-defined grid corresponds to the 15 element logarithm transform with one extra element located at 0.008.

A sensitivity analysis to this selectivity was performed to verify its influence on gas temperature at the outlet of the combustion chamber and at the outlet of the catalyst section.

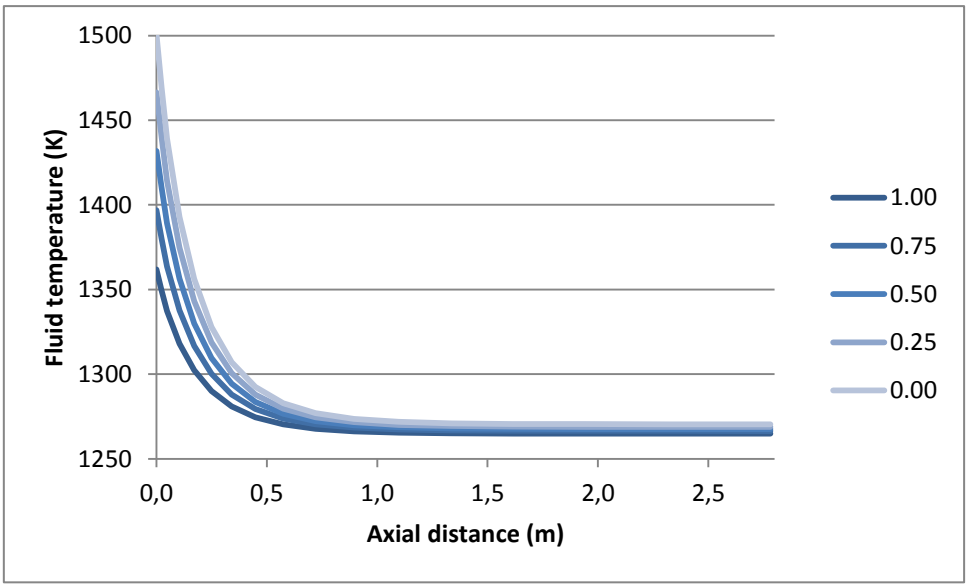

Figure 4.16 ATR combustion selectivity analysis, catalyst bed axial temperature profiles with varying CH_4/H_2 combustion reaction selectivity.

From this figure above, it is seen combustion reaction selectivity has mainly influence on fluid inlet temperature to the bed of catalyst. The predicted temperatures fall in the range reported in literature, 1373-1573 K [32]. Since there is no plant data available from the combustion zone this selectivity was chosen to be 1 that corresponds to the most general case.

Even though inlet temperature to the bed changes from 1360 K to 1500 K, there is practically no change to reactor outlet conditions. This is because the reactor model is always achieving equilibrium conditions and since it is an adiabatic vessel, the global energy balance remains unchanged.

4.2.3 Case I

Here results of the ATR simulation case study are presented, with the combustion chamber selectivity set to methane partial oxidation.

Table 4.18 ATR Case I combustion and catalyst zone outlet results.

	Plant data	Present work	Al-Dhfeery, 2012	units
Combustion zone				
Outlet T	-	1361.8	1369.8	K
Outlet P	-	32	32	bar
Catalyst zone				
Outlet T	1242.2	1264.8	1282.8	K
Outlet P	31.6	31.9	31.9	bar
Conversion	95.6%	97.4%	95.5%	
H_2/CO	4.39	4.45	4.44	
H_2/N_2	2.51	2.50	2.51	
$(H_2+CO)/N_2$	3.08	3.06	3.08	

Results shown in Table 4.18 reveal good prediction in terms of outlet composition and only slight deviations in temperature, pressure and conversion.

Outlet pressure difference relates to combustion zone and burner pressure drops, as well as inert catalyst sections inside the reformer. Outlet temperature deviations between this model and Al-Dhfeery and co-workers' model can relate to different thermodynamic physical properties model, but the deviation to plant data might relate to possible heat losses. ATR reformer vessels are considered to be adiabatic, but they operate at such high temperatures that a water cooling jacket may be used to stabilize external wall temperature (vide chapter 5 of [50]). In fact, Aasberg [32] refers that outer metal skin temperatures are reduced to 100-200 °C so it is possible that minor heat losses are present.

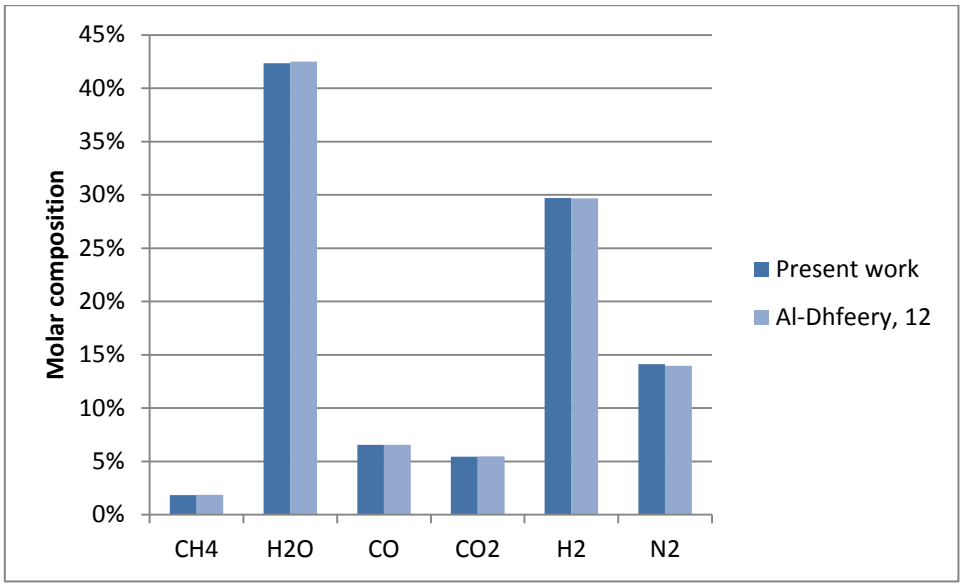

Figure 4.17 ATR Case I combustion zone outlet molar composition.

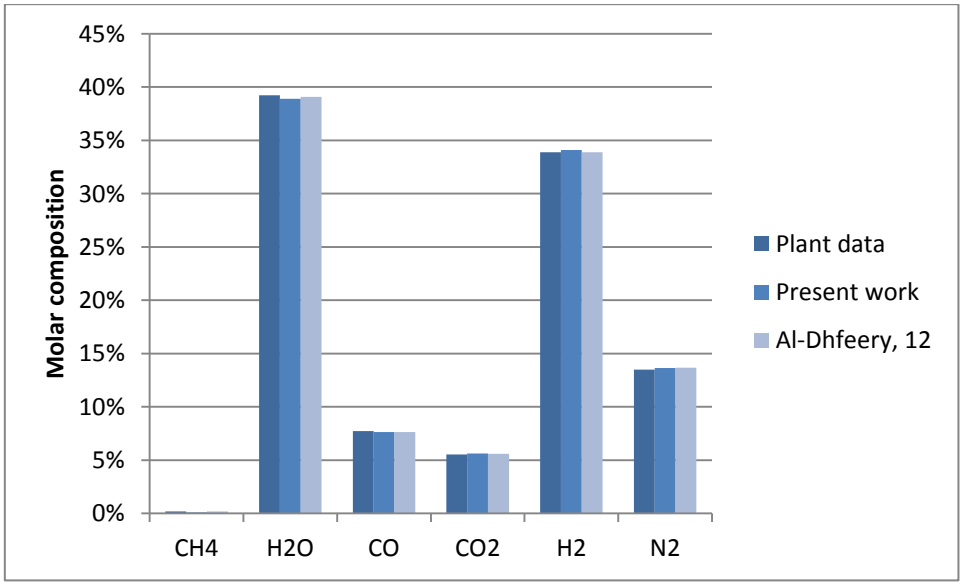

Figure 4.18 ATR Case I catalytic zone outlet molar composition.

Molar composition at combustion and catalyst zone outlets shows almost no difference with plant data or the paper's predictions, as it can be seen from Figure 4.17 and Figure 4.18.

Composition differences are very small, but the conversion values seem very different, with a relative error of 69%; this large relative error arises because of very low methane outlet contents. The difference in conversion comes from a low absolute error in terms of methane outlet content, $8x10^{-4}$.

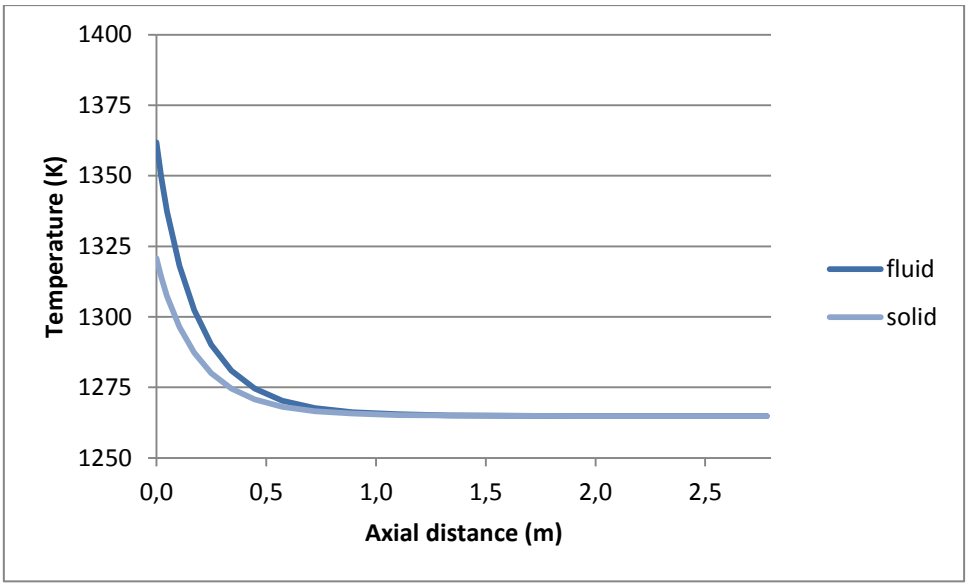

Figure 4.19 ATR Case I axial temperature profiles.

Figure 4.19 presents simulated fluid and solid axial temperature profiles. Since the reactor is adiabatic and reactions are endothermic, the flat profile suggests that almost only one third of the reactor is used for reaction. This profile is very different from the one predicted in the original paper, where the temperature drops along all the length of the reactor or, in other words, reaction happens along almost all reactor length. The difference might be related to different pellet models being used: one-dimensional pellet in this work, and pseudo-homogeneous in the original paper; and to lack of data for pellet properties, such as tortuosity, porosity or mean pore radius.

Al-Dhfeery and his co-workers used effectiveness factors of around 0.003, predicted from the Thiele modulus for spherical pellets, while the present model calculates effectiveness factors around 0.03, from detailed diffusion inside a hollow cylindrical pellet. This is a significant difference on the observed reaction rates; this profile could be adjusted by changing pellet tortuosity, porosity or mean pore radius from AML:FBCR default values to increase internal diffusion limitations, reducing reaction rates and thus flattening the temperature profiles.

The kinetic model and parameters used for this ATR catalyst were the same used for SMR modelling, but catalyst activity does not have to be the same for both catalysts. The catalyst from [10] had 15.2% Ni whereas in [20] has only 9% Ni; Max Appl in section 4.1.1.3.2 of [51] refers these ATR catalysts present 5-10% the activity of a SMR catalyst; so it is possible the real activity of the ATR catalyst is lower than the SMR catalyst. Without temperature measurements inside the reactor it's not possible to confirm how the reactor bed behaves.

Moreover, it is unlikely the reactor operates with two thirds of inactive bed. Other possible explanations could reflect that the catalyst bed is essential to stabilize the reaction mixture after the combustion zone and eliminate soot precursors to avoid soot formation in downstream equipment –

with this objective it is possible the catalyst bed is over-dimensioned and inactive to SR reactions to some extent.

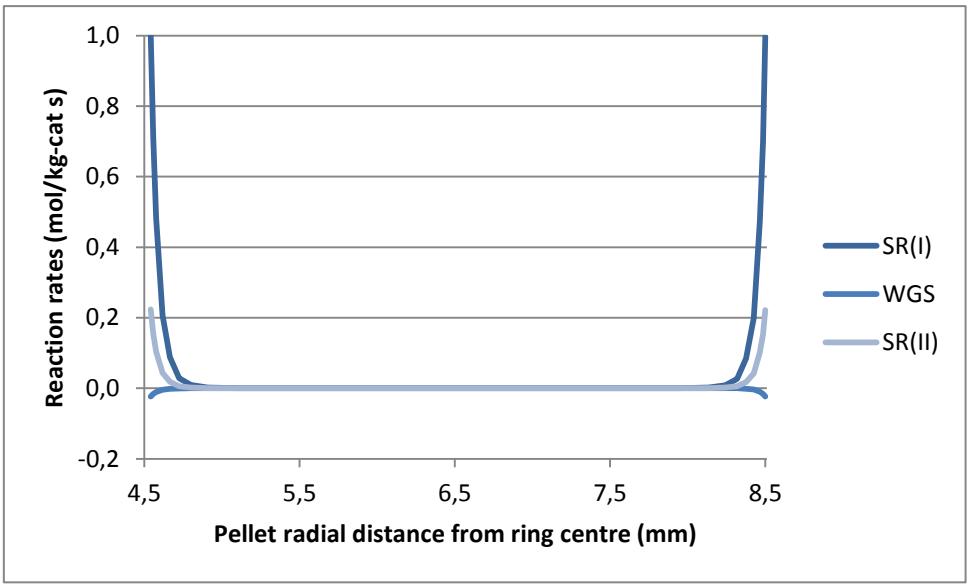

Figure 4.20 ATR Case I reaction rate pellet radial profiles.

Again, as occurred for SMR modelling, Figure 4.20 shows steep gradients of reaction near the pellet surface, which in this case is seen on both ends of the domain due to the hollow pellet shape. This also supports the importance of modelling SR reaction systems accounting for detailed diffusion of species inside catalyst particles

5 Steam Methane Reactor Optimisation

The Steam Methane Reactor (SMR) model used in section 4.1.4 with a fired heater model was used for operational conditions optimisation. The results predicted in that section were taken as the base case to be optimised. Initially in this section problem formulation is described and then results are presented and discussed.

5.1 Problem formulation

The reactor system from the original example was used for hydrogen production. This optimisation will thus try to maximise hydrogen production at a fixed natural gas feed flowrate. The objective function is:

$$f(x) = \max\left(F_{H_2}^{out}\right) \tag{5.1}$$

The control variables included in x are:

$$x = \left\{T^{in}, P^{in}, T_{eff}, S/C\ ratio\right\} \tag{5.2}$$

These correspond to four key design variables of the reactor: inlet temperature to the reactor tube, T^{in}; inlet pressure to the reactor tube, P^{in}; fired heater effective temperature, T_{eff}; and inlet $S/C\ ratio$.

The problem was subject to the following constraints:

$$max(T_w) < 1323.15\ K \tag{5.3}$$

$$max(\Delta P) < 5.52\ bar \tag{5.4}$$

Maximum wall temperature constraint reflects a material constraint described in section 2.4.1; and maximum pressure drop was assumed to be 120% of the base case scenario, for safety reasons.

The region where an optimal solution was searched for is defined by the following bounds on control variables:

$$673.15 < T^{in} < 923.15\ K \tag{5.5}$$

$$26 < P^{in} < 32\ bar \tag{5.6}$$

$$1500 < T_{eff} < 2000\ K \tag{5.7}$$

$$1.0 < S/C\ ratio < 6.0 \tag{5.8}$$

The upper bound on inlet temperature to the reformer can be regarded as an additional constraint as it reflects maximum feed temperature to avoid thermal cracking of higher hydrocarbons and carbon formation [36]. The fired heater effective temperature is an indirect model parameter for heating intensity. In real operation the fuel flowrate and air excess would be adjusted to get required process gas outlet temperature.

The optimisation problem had 109837 equations and 111261 variables. A total of 1420 variables were assigned and the remainder 4 degrees of freedom correspond to the four design variables

considered. The optimal solution was found in 499 seconds using an Intel® Core™ i7-3770S CPU with 16.0 GB of RAM.

5.2 Results and discussion

Optimisation results are summarised in Table 5.1 where hydrogen production increased by 30.9%. Active constraints are listed in Table 5.2.

Table 5.1 Optimisation results, objective function, control variables and KPI's.

	Base	Optimal	units
Objective function	3.287	4.346	mol/s
Control variables			
$\mathbf{T^{in}}$	793.15	923.15	K
$\mathbf{P^{in}}$	29	32	bar
$\mathbf{T_{eff}}$	1742.35	1872.04	K
S/C ratio	3.358	3.664	
KPI's			
Conversion	61.6%	86.3%	
$\mathbf{H_2/CO}$	7.89	5.66	
$\mathbf{T^{out}}$	1038.00	1143.92	K

Table 5.2 Active constraints and Lagrange multipliers.

Constrained variable	final value	units	Lagrange multiplier	constraint
$\mathbf{T_w}$	1323.15	K	$3.95 \cdot 10^{-3}$	(5.3)
ΔP	5.52	bar	$1.72 \cdot 10^{-6}$	(5.4)
$\mathbf{T^{in}}$	923.15	K	$4.84 \cdot 10^{-4}$	(5.5)
$\mathbf{P^{in}}$	32	bar	$1.22 \cdot 10^{-7}$	(5.6)

The optimiser tried to increase hydrogen production by increasing the energy provided for reaction, while keeping maximum wall temperature and pressure drop below their maximum values. This was accomplished on one hand, with an increase on inlet temperature, and a decrease on fired heater effective temperature to lower wall temperatures; and on the other hand, with an increase on inlet pressure to reduce the pressure drop and thus allow higher fluid temperatures[1].

The optimal solution stuck at inlet temperature and pressure upper bounds. It is interesting that while an inlet temperature increase would be expected, lower pressures would promote hydrogen production and methane conversion according to reaction (2.1). It seems the pressure drop effect described above prevailed over the thermodynamic effect on equilibrium. This upper bound on pressure drop should be reviewed with more detailed information about the maximum allowed pressure drop for the reformer in question.

[1] Higher pressures reduce the gas volume, thus reducing superficial velocities and pressure drop. A temperature increase has the opposite effect.

The Lagrange multipliers indicate the optimal solution sensitivity to changes on the respective control variables or constraints. In this case the highest value corresponds to the maximum wall temperature constraint (5.3), this means it is the most restrictive constraint, but it also suggests it will be difficult to control the unit's operation on this point, without violating this constraint.

Table 5.3 Energy demand increase, (compression duties neglected).

Energy demand increase	net (kW)	Relative
Furnace	79.3	30.4%
Feed preheating	49.3	39.3%
Total	128.6	33.3%

Hydrogen production and methane conversion increases of 32.2% and 40.2%, respectively, were accomplished by increasing energy use in both furnace and feed preheating. The total energy demand increase was 33.3% (see Table 5.3).

The optimised conditions reveal a slight energy efficiency decrease towards hydrogen production but a significant increase towards methane conversion. Table 5.4 shows the plant is spending 0.8% more energy per unit of hydrogen produced, E_{H2}, but 4.9% less per unit of methane converted, E_{CH4}.

Table 5.4 Energy consumption per mole of hydrogen produced, and per mole of methane converted.

E_{H2}	Base	Optimal	Change	units
Furnace	79.4	78.3	-1.4%	kJ/mol_{H2}
Feed preheating[2]	38.2	40.2	5.3%	kJ/mol_{H2}
Total	117.6	118.5	0.8%	kJ/mol_{H2}
E_{CH4}				
Furnace	295.1	274.6	-7.0%	kJ/mol_{CH4}
Feed preheating	142.0	141.0	-0.6%	kJ/mol_{CH4}
Total	437.1	415.6	-4.9%	kJ/mol_{CH4}

Also from Table 5.1 the optimised reactor produces a syngas with lower H_2/CO ratio. This extra carbon monoxide could be further processed in a water gas shift converter at lower temperatures, giving more hydrogen. The downside is that also more carbon dioxide will be co-produced in WGSR, and CO_2 cleaning processes will have a higher load to treat. Outlet molar compositions are compared in Figure 5.1.

[2] Considers the enthalpy change from pure components in the standard state to the process conditions.

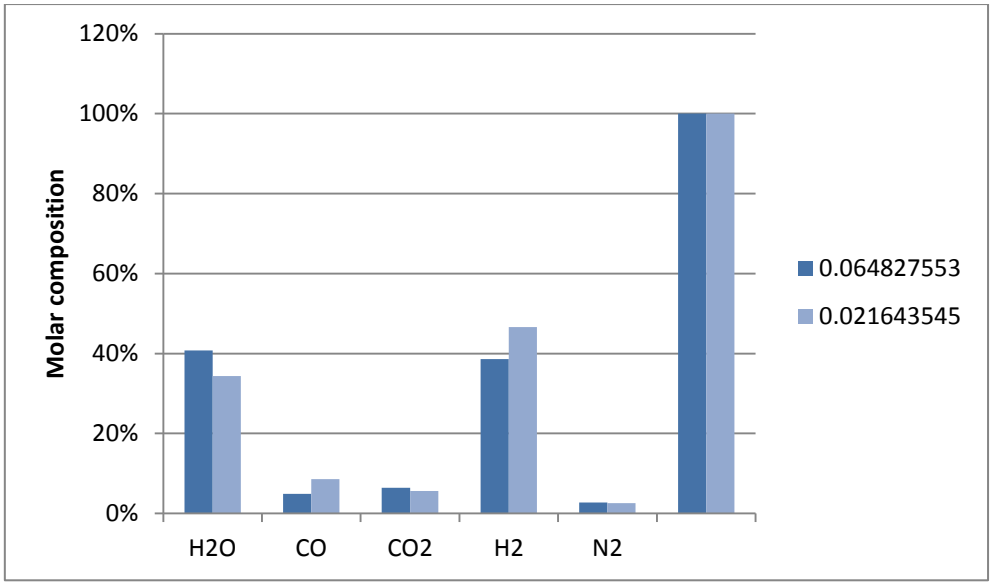

Figure 5.1 Base case and optimised SMR molar outlet composition.

5.3 Conclusions

Optimised conditions provide higher hydrogen production and methane conversion at the expense of higher energy demand. The global energy efficiency of the single reactor is slightly worse towards hydrogen production (more 0.9 kJ is spent per mole of H_2 produced) and somewhat better towards methane conversion (less 21.5 kJ spent per mole of methane converted).

The impact on downstream equipment is such that water gas shift converter section (WGSR) will handle more hydrogen production from CO, producing more energy from the exothermic reaction. This will lead to higher CO_2 contents that may need to be removed in the gas cleaning section. Upstream of the SMR a pre-reformer will be needed to allow reformer inlet temperatures of up to 923.15 K.

Since the WGSR section will convert more carbon monoxide to hydrogen more energy will be available for recovery. This should compensate the SMR energy efficiency decrease towards hydrogen production. The downside is that this heat will be recovered in the form of high or medium pressure steam and, in some cases, production of steam might be undesired.

In case the current reactor tube material cannot withstand temperatures of up to 1323.15 K, replacement of tubes could be an important decision factor for this optimisation. As wall temperature constraint is the most restrictive constraint, this would have a severe impact on this optimisation results. The Lagrange multiplier value for this constraint also suggests a control analysis is required before operating at the optimal value.

A further optimisation study of this reactor should consider a detailed firebox model to study how maximum wall temperature can be controlled and reduced, maybe by adjusting flame length. Or to allow a full design optimisation considering both furnace and reactor tube design parameters.

Related reactor sections and heat transfer integration could also be included to perform a flowsheet-level optimisation considering the effects on downstream and upstream units.

6 Conclusions

The two main natural gas reforming reactors (NGR), the steam methane reformer (SMR) and the autothermal reformer (ATR), were successfully modelled in gPROMS® using the Advanced Model Library for Fixed Bed Reactors (AML:FBCR), the Steady-State Process Model Library (PML:SS) and user-defined models.

Two different industrial cases were studied, one for SMR and another for ATR. Two approaches to model the SMR furnace side were used: one with fixed wall temperature profile (Case I) and the other with a fired heater (Case II). Both were able to predict the industrial case profiles and outlet conditions with some deviations on outlet composition and conversion due to model assumptions (e.g. ideal gas assumption on equilibrium calculations) or to inaccurate reported plant data (temperature, pressure and equilibrium composition).

The approach of modelling the ATR burner and combustion zone with a conversion reactor provided realistic inlet temperatures to the catalytic bed and reformer outlet composition is close to plant data and original paper predictions. Some temperature deviations between this work and the original paper predictions are present and possibly relate to different thermodynamic models being used in both works. Deviation from both model predictions and plant data possibly relate to small heat losses.

SMR predicted axial profiles are in agreement with the original paper. Predicted radial profiles show pronounced differences from tube centre to wall (e.g. temperature) even for small diameter tubes, which reveals the need for accurate two-dimensional bed models when diagnosing performance or designing this type of reactor and is in agreement with literature [32,33].

ATR predicted axial profiles deviate from the ones predicted in the original paper rendering almost two thirds of reactor bed inactive. Observed reaction rates in this paper's results are ten times lower than the predicted in this work, this difference arises because Al-Dhfeery, [20], used a simplified effectiveness factor and here a detailed multi-component diffusion approach was used to model the pellet. This model's profile could be adjusted by changing pellet tortuosity, porosity or mean pore radius. These parameters should be measured or adjusted to match plant data temperature profile measurements.

Pellet radial profiles predicted in both SMR and ATR cases demonstrate reactions are controlled by diffusion rates inside the pellet. The prediction of reaction rates and composition profiles inside the pellet affects the overall reactor performance. Detailed, one-dimensional, pellet models, accounting for multi-component diffusion inside the catalyst pores, is the only way of accurately predicting the phenomena occurring inside the catalyst particles, for this type of systems. The approach of pseudo-homogeneous models, where an effectiveness factor is calculated to predict the observed reaction rates inside the catalyst particles will not be able to predict the profiles shown in this work – see, for example, the discontinuity in WGS effectiveness factor in Figure 4.12.

In spite of the presence of light gases, that should show high diffusion rates, the reaction rates are even higher, rendering observed reaction rates below 10% of the intrinsic reaction rates; the fact that hydrogen and methane have very different diffusivities also supports this requirement for diffusion

modelling, as it forces a reaction like water gas shift proceed in one direction at catalyst surface, and in the reverse direction inside the catalyst particle – see Figure 4.11.

The SMR model was also successfully tested at different conditions to predict equilibrium conditions. While the ATR combustion chamber model was tested for different combustion reactions and predicted acceptable outlet temperatures.

Finally, the SMR model with the fired heater model was used for operational optimisation, where hydrogen throughput was maximised by increasing thermal preheating and furnace duties. The optimal solution revealed slightly less energy efficient operation towards hydrogen production, but considering total methane conversion, it revealed a more efficient operation.

6.1 Achievements

The objective of this work was to initiate development of models for NGR reactors with the purpose of creating accurate and predictive modelling solutions for hydrogen and synthesis gas manufacture in gPROMS®.

The two main reformers for NGR where modelled, considering rigorous mass and heat transfer inside the catalyst pellets. The SMR reactor bed was modelled with a two-dimensional, axially and radially distributed, model considering effective mass and heat transport.

The SMR furnace temperature profile was successfully predicted with a simplified radiation fired heater model. ATR burner and combustion zone were successfully modelled with a one-molecular methane partial oxidation reaction.

Two industrial case studies were simulated, one for the SMR and the other for the ATR. The SMR outlet conditions were successfully predicted with fixed wall temperatures and predicted heat fluxes from the fired heater mode. The ATR outlet conditions were predicted with some temperature deviations.

Finally, the operating conditions of the SMR industrial case were optimised using the detailed SMR reactor model with fired heater. This demonstrated that optimisation of complex accurate models can be used for optimisation in gPROMS®.

6.2 Future work

In order to further complete this work towards a comprehensive accurate and predictive modelling pack for synthesis gas manufacture there are still several steps to be taken.

Kinetics modelling can be improved by tackling the ideal gas assumption and implementing fugacity calculations. Steam reforming of higher hydrocarbons also needs to be considered. The undesired coking reactions can also be modelled.

The SMR furnace model needs to be improved, ideally accounting for detailed radiation and convection heat transfer. As a first step the fired heater could calculate the adiabatic flame temperature and energy balance from fuel composition and flowrate.

Modelling of NGR related equipment such as the pre-reformer and the WGSR will allow modelling of the complete NGR process. Developing models for other type of reactors like the heat exchanging reactors will provide different options for process design optimisation.

Finally, complete process modelling and optimisation, considering reactor or process design, with detailed high-fidelity models would be a proof of the power and capabilities of advanced process modelling to provide decision support and help achieving the best process innovation, design and operation decisions.

Bibliography

[1] J.R. Rostrup-Nielsen, T. Rostrup-Nielsen, Large-scale hydrogen production, CATTECH. 6 (2002).

[2] M. Linthwaite, T. Gamlin, Gas Conversion Using Novel Reforming Technology, 2000.

[3] International Energy Agency, Key World Energy Statistics, 2012.

[4] International Energy Agency, Gas Medium-Term Market Report, 2012.

[5] T.H. Fleisch, Syngas Chemistry: Key Technology for the 21st Century, 2006.

[6] J.R. Rostrup-Nielsen, Syngas in perspective, Catal. Today. 71 (2002) 243–247.

[7] K. Hou, R. Hughes, The kinetics of methane steam reforming over a Ni/Al2O catalyst, Chem. Eng. J. 82 (2001) 311–328.

[8] A.K. Avetisov, J.R. Rostrup-Nielsen, V.L. Kuchaev, J.B. Hansen, A.G. Zyskin, E.N. Shapatina, Steady-state kinetics and mechanism of methane reforming with steam and carbon dioxide over Ni catalyst, J. Mol. Catal. A Chem. 315 (2010) 155–162.

[9] J. Xu, G.F. Froment, Methane Steam Reforming, Methanation and Water-Gas Shift: I. Intrinsic Kinetics, AIChE J. 35 (1989) 88–96.

[10] J. Xu, G.F. Froment, Methane Steam Reforming : ll. Diffusional Limitations and Reactor Simulation, 35 (1989) 97–103.

[11] Z. Yu, E. Cao, Y. Wang, Z. Zhou, Z. Dai, Simulation of natural gas steam reforming furnace, Fuel Process. Technol. 87 (2006) 695–704.

[12] A. Olivieri, F. Vegliò, Process simulation of natural gas steam reforming: Fuel distribution optimisation in the furnace, Fuel Process. Technol. 89 (2008) 622–632.

[13] J.H. Ghouse, T.A. Adams Ii, A multi-scale dynamic two-dimensional heterogeneous model for catalytic steam methane reforming reactors, Int. J. Hydrogen Energy. 38 (2013) 9984–9999.

[14] P.M. Plehiers, G.F. Froment, Coupled Simulation of Heat Transfer and Reaction in a Steam Reforming Furnace, 12 (1989) 20–26.

[15] M.A. Soliman, S.S.E.H. Elnashaie, A.S. Al-Ubaid, A.M. Adris, Simulation of Steam Reformers for Methane, Chem. Eng. Sci. 43 (1988) 1801–1806.

[16] S.S.E.H. Elnashaie, A.M. Adris, M.A. Soliman, A.S. Al-Ubaid, Digital Simulation of Industrial Steam Reformers for Natural Gas Using Heterogeneous Models, Can. J. Chem. Eng. 70 (1992) 786–793.

[17] Y.-H. Yu, Simulation of Secondary Reformer in Industrial Ammonia Plant, Chem. Eng. Technol. 25 (2002) 307–314.

[18] J. Pina, D.O. Borio, Modeling and simulation of an autothermal reformer, Lat. Am. Appl. Res. 36 (2006) 289–294.

[19] K. Khorsand, K. Dehghan, Modeling and simulation of reformer autothermal reactor in ammonia unit, Pet. Coal. 49 (2007) 64–71.

[20] A. AL-Dhfeery, A. Jassem, Modeling and simulation of an industrial secondary reformer reactor in the fertilizer plants, Int. J. Ind. Chem. 3 (2012) 14.

[21] A.A. AL-Dhfeery, Evaluation Performance of Different Types Catalysts of an Industrial Secondary Reformer Reactor in the Ammonia Plants, Mod. Res. Catal. 01 (2012) 43–51.

[22] M.H. Sosna, Y.H. Yu, Modeling for Industrial Heat Exchanger Type Steam Reformer, Korean J. Chem. Eng. 18 (2001) 127–132.

[23] P. Stehlik, Radiative Component in Thermal Calculation of Tubular Heat Exchangers, Heat Transf. Eng. 16 (1995) 19–28.

[24] M.H. Wesenberg, Gas Heated Steam Reformer Modelling, Trodheim, Norway, 2006.

[25] J.K. Rajesh, S.K. Gupta, G.P. Rangaiah, A.K. Ray, Multi-objective optimization of industrial hydrogen plants, Chem. Eng. Sci. 56 (2001) 999–1010.

[26] A.D. Nandasana, A.K. Ray, S.K. Gupta, Dynamic Model of an Industrial Steam Reformer and Its Use for Multiobjective Optimization, Ind. Eng. Chem. Res. 42 (2003) 4028–4042.

[27] S. Choi, J. Park, C. Han, E.S. Yoon, Optimal Design of Synthesis Gas Production Process with Recycled Carbon Dioxide Utilization, Ind. Eng. Chem. Res. 47 (2008) 323–331.

[28] A. Behroozsarand, H. Ebrahimi, A. Zamaniyan, Multiobjective Optimization of Industrial Autothermal Reformer for Syngas Production Using Nonsorting Genetic Algorithm II, Ind. Eng. Chem. Res. 48 (2009) 7529–7539.

[29] H. Ebrahimi, A. Behroozsarand, A. Zamaniyan, Arrangement of primary and secondary reformers for synthesis gas production, Chem. Eng. Res. Des. 88 (2010) 1342–1350.

[30] J. Ellepola, N. Thijssen, J. Grievink, G. Baak, A. Avhale, J. Van Schijndel, Development of a synthesis tool for Gas-To-Liquid complexes, Comput. Chem. Eng. 42 (2012) 2–14.

[31] R.C. Baliban, J.A. Elia, C.A. Floudas, Novel Natural Gas to Liquids Processes : Process Synthesis and Global Optimization Strategies, AIChE J. 59 (2013) 505–531.

[32] K. Aasberg-Petersen, I. Dybkjær, C.V. Ovesen, N.C. Schjødt, J. Sehested, S.G. Thomsen, Natural gas to synthesis gas – Catalysts and catalytic processes, J. Nat. Gas Sci. Eng. 3 (2011) 423–459.

[33] J.R. Rostrup-Nielsen, Production of synthesis gas, Catal. Today. 18 (1993) 305–324.

[34] J.R. Rostrup-Nielsen, L.J. Christiansen, Concepts in Syngas Manufacture, Imperial College Press, 2011.

[35] I. Dybkjær, Tubular reforming and autothermal reforming of natural gas - an overview of available processes, Fuel Process. Technol. 42 (1995) 85–107.

[36] R. Reimert, F. Marschner, H.-J. Renner, W. Boll, E. Supp, M. Bejc, et al., Gas Production, 2. Processes, in: Wiley-VCH (Ed.), Ullmann's Encycl. Ind. Chem., 2012.

[37] J.N. Armor, The multiple roles for catalysis in the production of H2, Appl. Catal. A Gen. 176 (1999).

[38] H. Olsson, P. Rudbeck, K.H. Andersen, B.H. Olsson, P. Rudbeck, K.H. Andersen, Adding Hydrogen Production Capacity by Heat Exchange Reforming, 2007.

[39] R. Smith, A Review of the Water Gas Shift Reaction Kinetics, Int. J. Chem. React. Eng. 8 (2010).

[40] G.F. Froment, K.B. Bischoff, J. De Wilde, Chemical Reactor Analysis and Design, Wiley, 2010.

[41] E.N. Fuller, P.D. Schettler, J.C. Giddings, New method for prediction of binary gas-phase diffusion coefficients, Ind. Eng. Chem. 58 (1966) 18–27.

[42] B.E. Poling, J.M. Prausnitz, J.J.P. O'Connell, The Properties of Gases and Liquids, McGraw-Hill Education, 2001.

[43] R.W. Southworth, Chemical engineers' handbook, 4th ed., McGraw-Hill, New York, 1964.

[44] W. Reichelt, E. Blass, Fluidic Investigations of Packed Piped and Towers Filled with Raschig Rings, 1971.

[45] V.-G.V. und Chemieingenieurwesen, V.D.I. Gesellschaft, VDI Heat Atlas, Springer, 2010.

[46] S. Lögdberg, H.A. Jakobsen, Natural gas conversion - The Reforming and Fischer-Tropsch processes, n.d.

[47] J.K. Rajesh, S.K. Gupta, G.P. Rangaiah, A.K. Ray, Multiobjective Optimization of Steam Reformer Performance Using Genetic Algorithm, Ind. Eng. Chem. Res. 39 (2000) 706–717.

[48] K. Aasberg-Petersen, T.S. Christensen, C. Stub Nielsen, I. Dybkjær, Recent developments in autothermal reforming and pre-reforming for synthesis gas production in GTL applications, Fuel Process. Technol. 83 (2003) 253–261.

[49] P.S.E. Ltd., Pellet geometry settings in AML:FBCR, (2012).

[50] T. Uhde, Hydrogen, 2012.

[51] M. Appl, Ammonia - Principles and Industrial Practice, Wiley, 1999.